

國立臺灣大學理學院物理研究所

碩士論文

Graduate Institute of Physics

College of Science

National Taiwan University

Master Thesis



寬度引發的不均勻性對石墨烯傳導的影響

The impact of width-induced inhomogeneity on the carrier
transport in graphene system

楊維元

Wei-Yuan Yang

指導教授: 梁啟德博士

Advisor: Chi-Te Liang, Ph.D.

中華民國 104 年 7 月

July, 2015

國立臺灣大學碩士學位論文

口試委員會審定書

寬度引發的不均勻性對石墨烯傳導的影響

The Impact of Width-Induced Inhomogeneity on the Carrier
Transport in Graphene System

本論文係楊維元君 (R02222025) 在國立臺灣大學物理學系所完成之碩士學位論文，於民國 104 年 7 月 20 日承下列考試委員審查通過及口試及格，特此證明

口試委員：

梁啟德

(簽名)

(指導教授)

林立弘

梁啟德

杭大仁



致謝

由衷地感謝我的指導教授梁啟德在碩士兩年的指導與協助。碩士兩年的過程中，老師給予我們研究方向的指點、研究能力的培養以及待人處事上的指引。儘管老師在碩二的時候出國訪問學者一年，老師對於實驗上的事情仍極力給予協助與幫忙、詢問國外實驗室是否有解決的辦法... 等。

碩一時，謝謝翊亭、泛鴻、承華學長及新竹陳正中老師及九君學長的教導，讓我更進一步熟稔低溫半導體領域及實驗上層面的思考。

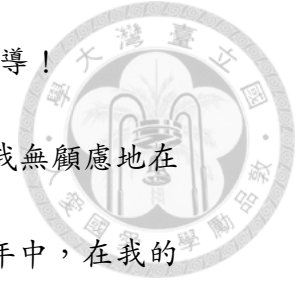
感謝兩年的好隊友稟弋在新竹以及台北的量測，相信我們以後見面一定能回想起那時一起量測、製作樣品所遇到的點點滴滴。感謝舜聰學長在這次的研究上給予極大的協助與支持，也謝謝學長不辭辛勞地從台南來台北給予實驗上的建議與物理上的討論。誠摯地感謝學長的幫忙。

也感謝實驗室同學政榮、侑凡、英廷、仕卿給予實驗上適時的協助及物理上的分析與討論。除此之外也感謝德邦學長在物理上的討論，

也謝謝馨彥學長在程式上的指點與幫忙及論文寫作上的指導！

最後，誠心地感謝我爸爸媽媽在這兩年的時光中，讓我無顧慮地在台北做我想做的事情。也謝謝我女朋友林文心，在這兩年中，在我的身後支持我、協助我，感謝您包容我這兩年來的壞脾氣。

碩士的生涯在口試的那天告一段落了，祝之後的學弟妹們（雅琪、宜儒）及稟弋、玠沂、玠汶... 等實驗室的同學們在研究路上一切順心如意。






中文摘要

自 2004 年以來，石墨烯材料被機械式剝離法取得之後，引發學界的高度興趣。由於石墨烯具有高導電、導熱以及高載子遷移率的特性，很多的研究專注於研究高載子遷移率下的費米子傳輸行為。然而，低遷移率的石墨烯仍具有高度的潛力。在很多研究中指出，由於雜質摻雜所造成的低載子遷移率的石墨烯樣品上可以觀察到能隙被打開的現象。在本篇論文中，我著重於導電通道的寬度對於無序性石墨烯樣品的影響。

藉由光蝕刻技術，我們把樣品製作成標準的四點量測形狀 (Hall bar pattern)。其中導電通道的寬度分別為 1.25、5.90 以及 25.09 μm 。我們逐步量測從 2 K 到 30 K 電流對電壓的關係圖，其中樣品在溫度低的區間中展現出高度的非線性，而此非線性區域與 Variable range hopping 的電子傳輸機制有高度的關聯性。在不同寬度的樣品中，我們發現導電通道較寬的樣品上適用這個模型。因此我們推測寬度較窄的樣品可能存在某種機制導致電性傳輸比寬的樣品好。此現象也可以藉由電流



密度對電壓的關係圖中展現出來，較窄的樣品中面電流遠大於較寬的樣品。透過拉曼分析表面的雜質強度，我們發現到雖然摻雜的濃度相同，但是在窄的樣品上不均勻性較高。此不均勻性反而使整體的導電性增加。

此份研究嘗試了不同寬度的導電通道在無序性石墨烯樣品上的研究，在未來的展望中，可以測量高載子遷移率的樣品下傳導的差異性以及不同寬度的石墨烯樣品在磁場下載子傳輸的影響。

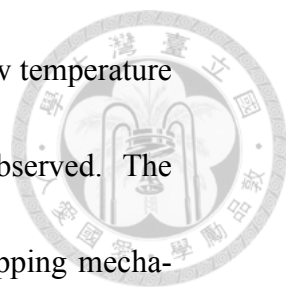
關鍵字：石墨烯、多重寬度的窄橋結構、邊緣效應、不均勻性、化學氣相沈積、雙極性電場效應、Mott variable range hopping (VRH)



Abstract

Ever since graphene, a single layer of graphite, was realized experimentally by the mechanically exfoliated method in 2004, it has become a major field of interest in the condensed matter physics. It has many fascinating properties, such as high electric conductivity, thermal conductivity, and mobility, etc. Also, with the features of massless fermion as carriers, many researches have been focused on the investigation in high-mobility graphene devices. On the other hand, low-mobility ones also show great potential with an opened band gap and other impurities-scattering effects. In this thesis, we focus on the width effect in a disordered graphene system to its electronic transport properties.

By using processes involving a photolithography method, we patterned our chemical vapor deposited (CVD) graphene into devices with different channel width Hall bars. The channel widths of our devices are 1.25, 5.90, and 25.09 μm respectively. Current-voltage (I - V) measurements were performed



from 2 K to 30 K with a 2 K temperature increment. At the low temperature region, the nonlinear I - V curve at the low field region was observed. The resistance-temperature (R - T) diagrams, which reveals the hopping mechanism within each channel, was derived through differentiating the inversed slope of the I - V diagrams. By comparing the R - T diagrams among three devices, the one with narrowest channel width was found to have the highest current density. Combing these results with the standard deviation of impurity strengths acquired from Raman spectroscopy, we conclude that the width induced inhomogeneity in a graphene system can act as a major impact on its electronic transport behavior.

Our work opens the door to the study of graphene samples with different channel widths. More works could be investigated in the near future, including subjects regarding high-mobility samples and the transport under a vertical magnetic field. Other intrinsic effects may come out to complete the whole picture on the transport behavior of this fascinating material.

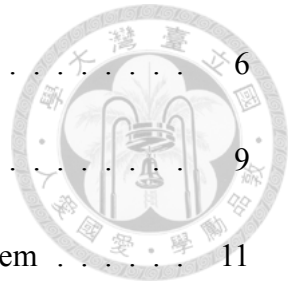
Key words: graphene, multi-width narrow bridge, edge effect, inhomogeneity, ambipolar field effect, Mott variable range hopping (VRH).



Contents

口試委員會審定書	i
致謝	ii
中文摘要	iv
Abstract	vi
Contents	viii
List of Figures	xi
List of Tables	xvii
1 Introduction	1
1.1 Pristine Graphene and Disordered Graphene	1
1.2 Organization	3
2 Theoretical Background Knowledge	6

2.1	Graphene Zero-Gap Band Structure	6
2.2	Drude model	9
2.3	Tunable carrier concentration and mobility in graphene system	11
2.4	Strong Localization	13
3	Sample Fabrication	17
3.1	Graphene Transfer Technique	17
3.2	Hall-bar patterning	18
3.3	Sample packaging	20
4	Experimental Techniques	21
4.1	Raman spectroscopy	21
4.2	Scanning electron microscopy	25
4.3	Cryogenic system	26
4.4	Four-terminal resistance measurement	29
5	Transport through CVD-Grown Graphene Constrictions	33
5.1	Ambipolar Field Effect and Nonlinear I - V Curves	35
5.2	VRH Model for Three Devices	40
5.3	Inhomogeneous Impurities Effect	42
5.4	Transport Gap and Transition from Intermediated to High-Field Expression	46



6 Conclusion

A Nonlinear I-V Curve for each Device

B Temperature Dependence on the Conductance for D3

C Strength of disorder by Raman spectroscopy

54

56

62

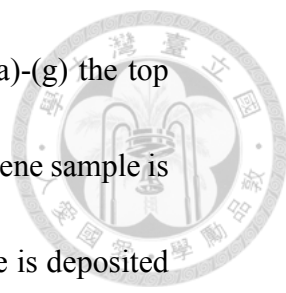
64





List of Figures

2.1	Schematic diagram of graphene lattice structure.	7
2.2	Schematic band structure of Single layer graphene. Right picture shows the zero-band gap of graphene near K point.	8
2.3	Schematic diagram of electron transport in the Drude model.	10
2.4	Schematic diagram of the two-plate model	11
2.5	Schematic diagram showing Variable range hopping. When the tempera- ture is low enough, jumping to further site is much easier than the nearest one. (a) and (b) are NNH and VRH model respectively.	13



3.1 The cartoon diagram of our photolithography processes. (a)-(g) the top view and the side view of each process (a) At first, the graphene sample is transferred to the SiO₂/Si substrate. (b) The photoresistance is deposited on the sample via spin coating method. (c) The sample is exposed under the UV light with our optical mask. (e) the sample has been developed with the TMAH solution and etched by the O₂ plasma. (f) the final pattern of the hall bar (g) Au/Ti film is then deposited on it respectively. 19

3.2 The top view of the sample and the system holder. 20

4.1 a schematic diagram of the light scattering process. 22

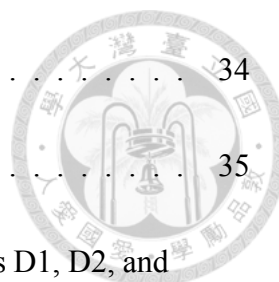
4.2 Illustration of Raman energy state for Rayleigh, Stokes, anti-Stokes Raman process. The electron will jump to the virtual state and then go back to the lower energy state coming with the emission light. 24

4.4 Side view of the Triton system. 27

4.5 Schematic view of the system showing the main heat exchange mechanism. the pre-cooling circuit is shown in red and the dilution circuit in green.[1] 28

4.6 The phase diagram of ³He/⁴He phase diagram.[2] 28

4.7 Illustration diagram of van der Pauw electrical configuration. The resistance $R_{mn,op}$ is defined as V_{mn}/I_{op} [3] 31



5.1 SEM picture of all the samples on a chip. 34

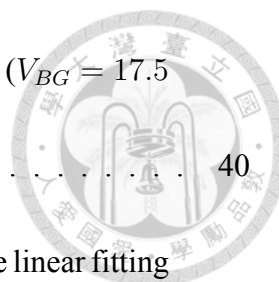
5.2 The configuration of the four-terminal measurement. 35

5.3 SEM picture of each device. From top to bottom are label as D1, D2, and D3 in sequence. The channel widths of each device are 1.25, 5.90, 25.09 μm respectively. 36

5.4 Resitivity R at low bias field versus V_{BG} , defined as dV/dI , at different back gate voltage. The Dirac point of three devices are around 17.5 V, which means that doping level is the same. At V_{BG} lower than 17.5 V is in hole region and on the otherside (higher than 17.5V) is in electron region. . . . 37

5.5 I - V curves for D3 at 30K. (a) and (b) are in the hole and the electron region respectively. The back gate voltage is set at $-2.5, 0, 2.5, 5, 7.5, 8.75, 10, 11.25, 12.5, 13.75, 15, 16.25, 17.5$ V from left to right for figure a; $17.5, 18.75, 20, 21.25, 22.5, 23.75, 25, 27.5, 30, 32.5, 35, 37.5$ V from right to left for figure b. 38

5.6 I - V curves for the D3 at 2 K. (a) and (b) are in the hole region and in the electron region respectively. The back gate voltage is set at $-2.5, 0, 2.5, 5, 7.5, 8.75, 10, 11.25, 12.5, 13.75, 15, 16.25, 17.5$ V from left to right for figure a; $17.5, 18.75, 20, 21.25, 22.5, 23.75, 25, 27.5, 30, 32.5, 35, 37.5$ V from right to left for figure b. 39



5.7 Temperature dependence of $I-V$ curve at the neutrality point ($V_{BG} = 17.5$ V) for D3. 40

5.8 Semi-log plot of the conductance versus the temperature. The linear fitting method is applied to three devices in view of the VRH model. 41

5.9 Schematic diagram of the position of Raman signal. 43

5.10 Cartoon diagram showing that the impact of impurities on the band structure of graphene.(a) and (b) are for the homogeneity and inhomogeneity cases respectively. Because D1 is much more inhomogeneous than D3, D1 and D3 are related to case b and a respectively. 45

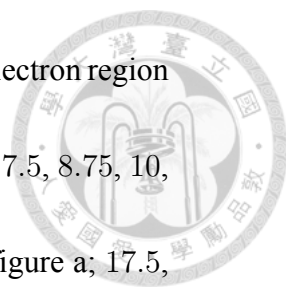
5.11 $I-V$ curve and $J-V$ curve for each device at the neutrality point. 45

5.12 Characteristic temperature T_m versus voltage relative to Dirac point $V - V_{Dirac}$ for D3. 47

5.13 $\ln G$ versus V_{xx} at different temperature for D3. The red and green lines in the diagram are the fitting curve for Pollak-Riess and Shklovskii expression respectively. 49

A.1 Temperature dependence for D1 at the neutrality point ($V_{BG} = 16.25$ V). 56

A.2 Temperature dependence for D2 at the neutrality point ($V_{BG} = 17.5$ V). . 57

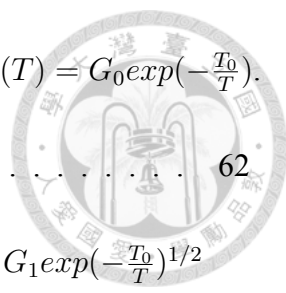


A.3 *I-V* curves for D1 at 30K. (a) and (b) are in the hole and the electron region respectively. The back gate voltage is set at $-2.5, 0, 2.5, 5, 7.5, 8.75, 10, 11.25, 12.5, 13.75, 15, 16.25, 17.5$ V from left to right for figure a; $17.5, 18.75, 20, 21.25, 22.5, 23.75, 25, 27.5, 30, 32.5, 35, 37.5$ V from right to left for figure b. 58

A.4 *I-V* curves for D2 at 30K. (a) and (b) are in the hole and the electron region respectively. The back gate voltage is set at $-2.5, 0, 2.5, 5, 7.5, 8.75, 10, 11.25, 12.5, 13.75, 15, 16.25, 17.5$ V from left to right for figure a; $17.5, 18.75, 20, 21.25, 22.5, 23.75, 25, 27.5, 30, 32.5, 35, 37.5$ V from right to left for figure b. 59

A.5 *I-V* curves for D1 at 2K. (a) and (b) are in the hole and the electron region respectively. The back gate voltage is set at $-2.5, 0, 2.5, 5, 7.5, 8.75, 10, 11.25, 12.5, 13.75, 15, 16.25, 17.5$ V from left to right for figure a; $17.5, 18.75, 20, 21.25, 22.5, 23.75, 25, 27.5, 30, 32.5, 35, 37.5$ V from right to left for figure b. 60

A.6 *I-V* curves for D2 at 2K. (a) and (b) are in the hole and the electron region respectively. The back gate voltage is set at $-2.5, 0, 2.5, 5, 7.5, 8.75, 10, 11.25, 12.5, 13.75, 15, 16.25, 17.5$ V from left to right for figure a; $17.5, 18.75, 20, 21.25, 22.5, 23.75, 25, 27.5, 30, 32.5, 35, 37.5$ V from right to left for figure b. 61



B.1 $\ln G$ versus T^{-1} by thermal activated model, which follows $G(T) = G_0 \exp(-\frac{T_0}{T})$.

..... 62

B.2 $\ln G$ versus $T^{-1/2}$ by ES VRH model, which follows $G(T) = G_1 \exp(-\frac{T_0}{T})^{1/2}$
for 2D system. 63

B.3 $\ln G$ versus $T^{-1/3}$ by Mott VRH model, which follows $G(T) = G_2 \exp(-\frac{T_0}{T})(1/3)$.
..... 63

C.1 The intensity of the disorder by Raman spectroscopy for D1. An offset
has been added to in order to separate each line. The value of I_D/I_G for
each line is labels on the graph. 64

C.2 The intensity of the disorder by Raman spectroscopy for D2. An offset
has been added to in order to separate each line. The value of I_D/I_G for
each line is labels on the graph. 65

C.3 The intensity of the disorder by Raman spectroscopy for D3. An offset
has been added to in order to separate each line. The value of I_D/I_G for
each line is labels on the graph. 65



List of Tables

5.1 Collected data for the strength of disorder, defined as I_D/I_G , at each position. Original Raman data are attached in the appendix C. 43



Chapter 1

Introduction

Field effect transistors (FET) play an important role in the semiconductor industry. By using the band gap of a semiconductor to represent 0 and 1 in logic computing, it makes a great breakthrough in the data processing of the modern society. Silicon-based semiconductor industry is going to meet its limitation owing to the current heating problem and its low mobility [1]. However, Graphene, an ideal two-dimensional (2D) system, exhibit excellent electrical and thermal conductivity [2, 3], which attracts many researchers in the world to engage themselves in investigating this novel material.

1.1 Pristine Graphene and Disordered Graphene

Graphene, a two dimensional allotrope of carbon, was first realized experimentally by Geim's group in 2004 [2]. It has been regarded as an unstable structure due to the

Mermin-Wigner theorem which reveals that 2D crystals only exist at zero temperature [4].

The first graphene device was fabricated through exfoliated method. Other fabricated methods are also invented in recent years such as chemical vapor deposition (CVD) [5] and epitaxial growing method [6]. Due to its genuine 2D structure and other fascinating features, many research works have been investigated such as weak anti-localization [7], fractional quantum Hall effect [8], ballistic transport in Graphene [9], barrier tunneling for massless carrier (Klein paradox) [10, 11] etc. These kinds of physical phenomena require ultra-high quality graphene samples. On the other hand, researchers also showed great interests in low-quality graphene samples such as nitrogen doped graphene [12], hydrogenated graphene [13, 14], and reduced graphene oxide (rGO) [14].

For low-quality graphene samples, it provides an entry to the strong localization of the charge carriers and the hopping behavior in the carrier transport [13, 15–17]. These kinds of phenomena are uncommon in pristine graphene samples. Besides these features, the most fascinating effect is that there exists transport gap in a disordered graphene system. Due to this transport gap, which cannot be observed in the pristine graphene with zero-band gap, graphene FET devices [18] can be possibly realized. Thus, some graphene-based transistor such as graphene nanoribbons [19] and rGO devices have been fabricated to take a deep sight into its transport behavior.

1.2 Organization

In our experiment, we fabricated different channel widths of chemical vapor deposition (CVD) graphene devices to investigate their impacts of the channel width on the electrical transport. The organization of this thesis is as follows. In chapter 2, the band structure of graphene and the properties of two dimensional electron gas (2DEG) will be included. In chapter 3, the method of sample fabrication and the experiment detail are included. Chapter 4 contains the experiment instruments such as Raman spectroscopy and scanning electron microscopy. Other experiment results and discussion would be explained in chapter 5 and 6.





Bibliography

- [1] W. Wondrak, *Microel. Rel.* **39**, 1113 (1999).
- [2] A. Geim and K. Novoselov, *Nat. Mater.* **6**, 183 (2007).
- [3] K. S. Novoselov, A. K. Geim, S. V. Morozov, D. Jiang, S. V. D. M. I. Katsnelson, I. V. Grigorieva, and A. A. Firsov, *Nature* **438**, 197 (2005).
- [4] R. C. Thompson-Flagg, *Europhys. Lett.* **85**, 46002 (2009).
- [5] Y. Zhang, L. Zhang, and C. W. Zhou, *Acc. Chem. Res.* **46**, 2329 (2013).
- [6] H. Tetlow, J. P. de Boer, I. J. Ford, D. D. Vvedensky, J. Coraux, and L. Kantorovich, *Phys. Rep.* **542**, 195 (2014).
- [7] X. S. Wu, X. B. Li, Z. M. Song, C. Berger, and W. A. de Heer, *Phys. Rev. Lett.* **98**, 136801 (2007).
- [8] X. Du, S. I. F. Duerr, A. Luican, and E. Y. Andrei, *Nature* **462**, 192 (2009).
- [9] J. Baringhaus, M. Ruan, F. Edler, A. Tejada, M. Sicot, Taleb-IbrahimiAmina, A.-P.

Li, Z. Jiang, E. H. Conrad, C. Berger, C. Tegenkamp, and W. A. de Heer, *Nature* **506**, 349 (2014).



- [10] M. I. Katsnelson, K. S. Novoselov, and A. K. Geim, *Nat. Phys.* **2**, 620 (2006).
- [11] L. Dell'Anna and A. D. Martino, *Phys. Rev. B* **79**, 045420 (2009).
- [12] Y. F. Lu, S. T. Lo, J. C. Lin, W. Zhang, J. Y. Lu, F. H. Liu, C. M. Tseng, Y.-H. Lee, C.-T. Liang, and L.-J. Li, *Nano Lett.* **7**, 6522 (2013).
- [13] S.-T. Lo, C. Chuang, R. K. Puddy, T.-M. Chen, C.-G. Smith, and C.-T. Liang, *Nanotechnology* **24**, 165201 (2013).
- [14] D. Joung and S. I. Khondaker, *Phys. Rev. B* **86**, 235423 (2012).
- [15] S. Z. Liang and J. O. Sofo, *Phys. Rev. Lett.* **109**, 256601 (2012).
- [16] C. Y. Cheah, C. Gómez-Navarro, L. C. Jaurigue, and A. B. Kaiser, *J. Phys.-Condens. Mat.* **25**, 465303 (2013).
- [17] D. Joung, L. Zhai, and S. I. Khondaker, *Phys. Rev. B* **83**, 115323 (2011).
- [18] B. Standley, A. Mendez, E. Schmidgall, and M. Bockrath, *Nano Lett.* **12**, 1165 (2012).
- [19] J. Bai, R. Cheng, F. Xiu, L. Liao, M. Wang, A. A. Shailos, K. L. Wang, Y. Huang, and X. F. Duan, *Nat. Nano.* **5**, 655 (2010).



Chapter 2

Theoretical Background Knowledge

2.1 Graphene Zero-Gap Band Structure

Carbon has four valence electrons around the nuclei. For the structure of graphene, s , p_x and p_y orbitals are hybridized into sp^2 orbital, which form σ bonds to connect the nearest three atoms. The P_z orbital, otherwise, form a π bond. The electron in P_z orbital is delocalized and is the main conducting carriers that can travel around each atom.

The lattice structure of graphene is shown in figure 2.1 and it is a honeycomb lattice. This kind of lattice is not a standard Brillouin lattice. Therefore, the best way to calculate the band structure is to separate the lattice into two sublattices (the orange one and the green one in the figure). By using Bloch's theorem, we can select two Bloch orbitals as

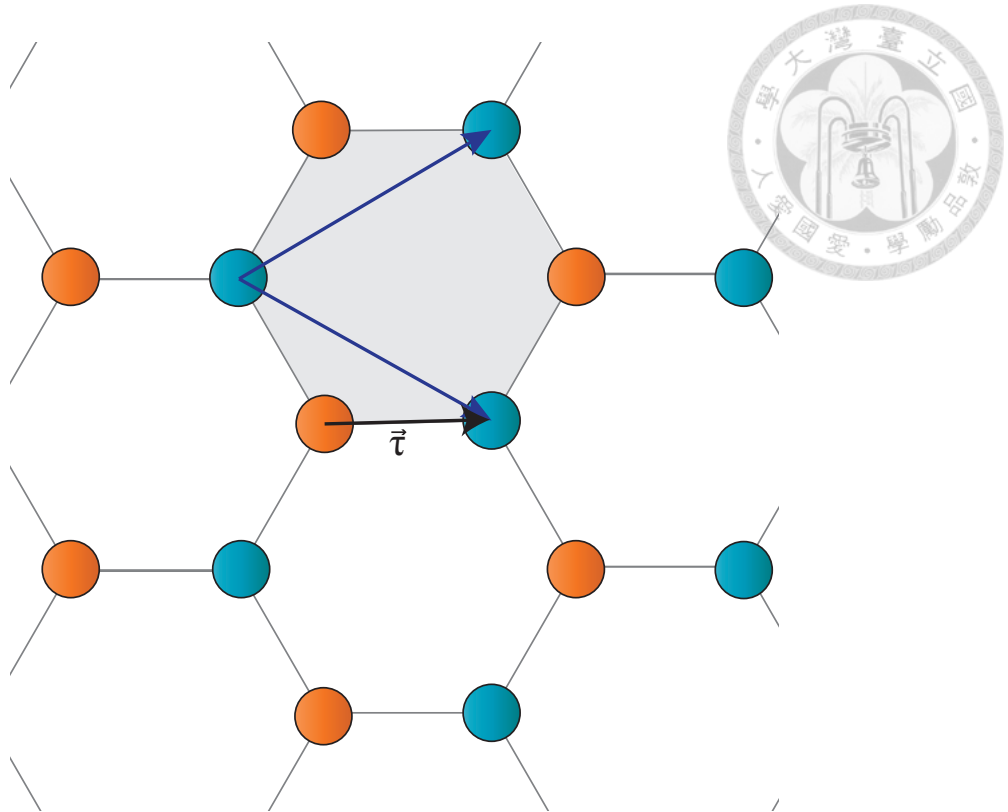


Figure 2.1: Schematic diagram of graphene lattice structure.

the basis.

$$|\vec{k}A\rangle = \frac{1}{\sqrt{N}} \sum_{\vec{R}} e^{i\vec{k}\vec{R}} |\vec{R}\rangle \quad (2.1a)$$

$$|\vec{k}B\rangle = \frac{1}{\sqrt{N}} \sum_{\vec{R}} e^{i\vec{k}\vec{R}} |\vec{R} + \tau\rangle \quad (2.1b)$$

Where $\vec{\tau}$ is the vector between two sublattices as defined in figure2.1, $|\vec{k}A\rangle$ and $|\vec{k}B\rangle$ are the basis function of two sublattices. With the help of the tight-binding (TB) model, the

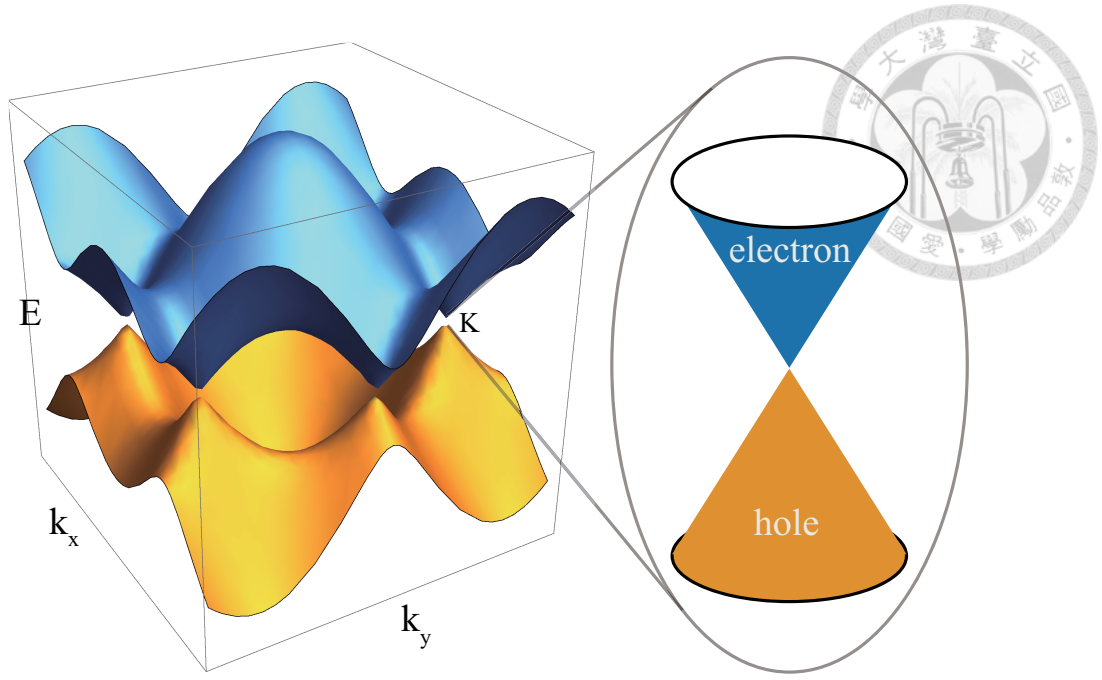


Figure 2.2: Schematic band structure of Single layer graphene. Right picture shows the zero-band gap of graphene near **K** point.

Hamiltonian \hat{H} can be written as

$$\hat{H}(\hat{k}) = \begin{pmatrix} 0 & e(\mathbf{k}) \\ e^*(\mathbf{k}) & 0 \end{pmatrix}, \quad (2.2)$$

where $|e(\mathbf{k})| = \pm t \sqrt{1 + 4\cos(\frac{\sqrt{3}k_x a}{2})\cos(\frac{k_y a}{2}) + \cos^2(\frac{k_y a}{2})}$, t is the hopping matrix element, and a is the distance between two carbon atoms.

The energy of the band structure is plotted in Figure 2.2. The energy band near the boundaries of Brillouin zone is unique, **K** point in the figure, which has caused a lot of interests. By substituting $\delta\mathbf{k} = \mathbf{k} - \mathbf{K}$ into the equation, the Hamiltonian can be written

as a form of Weyl Hamiltonian (Dirac equation for massless fermions).



$$\hat{\mathbf{H}}(\delta\hat{k}) = -V_F\hat{\sigma} \cdot \vec{p}, \quad (2.3)$$

where $V_F \approx \frac{c}{300}$ is the Fermi velocity of the carriers, $\hat{\sigma}$ is the Pauli matrix and \vec{p} is the momentum of the carriers. The energy band near \mathbf{K} is a conical band structure which is a zero-band gap and the Fermi velocity of the carriers is near the speed of the light.

2.2 Drude model

The carrier transport in condensed matter physics can be well described by the Drude model. It was revealed by Paul Drude in 1900 [1]. This model assumes that all atoms lose its valence electrons and that those atoms become positive charged ions. Therefore, the free electrons will collide with the charged ions as they transport through the conducting channel (see Figure 2.3).

In this model, Drude claimed that in the electron transport there exists a relaxation time τ , which represents the average collision time, such that the average velocity can be expressed by

$$\langle v \rangle = \frac{eE\tau}{m^*}, \quad (2.4)$$

where e is the electron charge, $\langle v \rangle$ is the average velocity, and E is the external electric

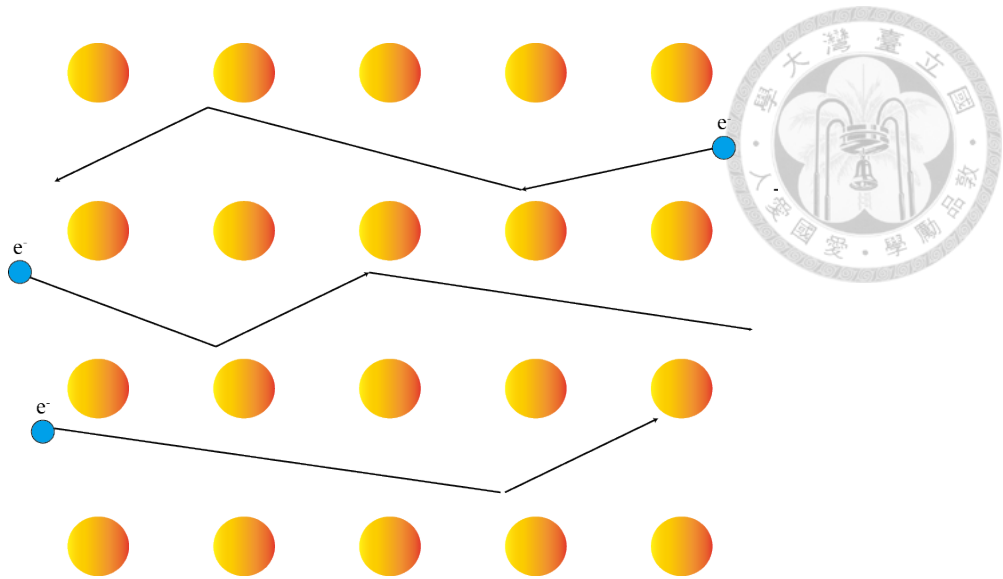


Figure 2.3: Schematic diagram of electron transport in the Drude model.

field. Also, current velocity J can be written as

$$J = ne \langle v \rangle, \quad (2.5)$$

where n is the charge density. Combining equation 2.4 and 2.5 with the Ohm's law:

$$J = \sigma E, \quad (2.6)$$

where σ is the conductivity. The electron conductivity can be obtained

$$\sigma = \frac{ne^2\tau}{m^*} \quad (2.7)$$

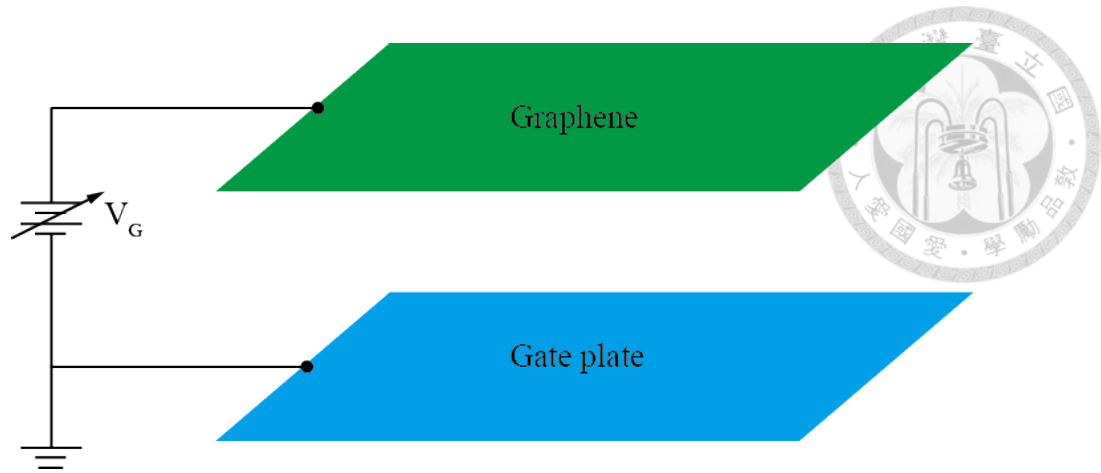


Figure 2.4: Schematic diagram of the two-plate model

2.3 Tunable carrier concentration and mobility in graphene system

Inside a semiconductor, the charge concentration can be altered by both chemical and electrical method. For example, the concentration of doping IIIA (VB) element in silicon affects the major charge carriers. This belongs to the first type. However, this kind of method is irreversible. As for the second kind, the same purpose can be achieved in a reversible way by using a gate electrode on the sample surface, bottom or top.

The mechanism of varying carrier concentration can be explained as follows. A parallel-plate model can be well explained the physical mechanism. In figure 2.4, the capacitance can be written as

$$C = \frac{\epsilon A}{d}, \quad (2.8)$$

where A is the area of the sample, d is the distance between the gate plate and graphene, and ϵ is the permittivity of the material (SiO_2 for our case). Note that the capacitance is

defined as $Q = C\Delta V$. Thus, the relationship between back gate voltage and the charge concentration is

$$neA = \frac{\epsilon A}{d}V_G \quad (2.9)$$

For graphene, the minimum charge concentration occurs at Dirac point also named as neutrality point. Thus, the relationship between the charge concentration and the back gate voltage can be rewritten as

$$ne = \frac{\epsilon}{d}(V_G - V_{dirac}) \quad (2.10)$$

Note that the mobility μ is defined as

$$\sigma = ne\mu, \quad (2.11)$$

where σ is the conductivity and n is the carrier concentration. With equation 2.5, 2.10, and 2.11, the mobility of graphene can be derived as

$$\mu = \frac{1}{R_{xx}C_{SiO_2}(V_G - V_{dirac})} \times \frac{L}{W}, \quad (2.12)$$

where W and L are the width and the length of the conducting channel respectively. Thus, the mobility and the charge concentration in graphene can be altered by the back gate

voltage and this is a reversible process.



2.4 Strong Localization

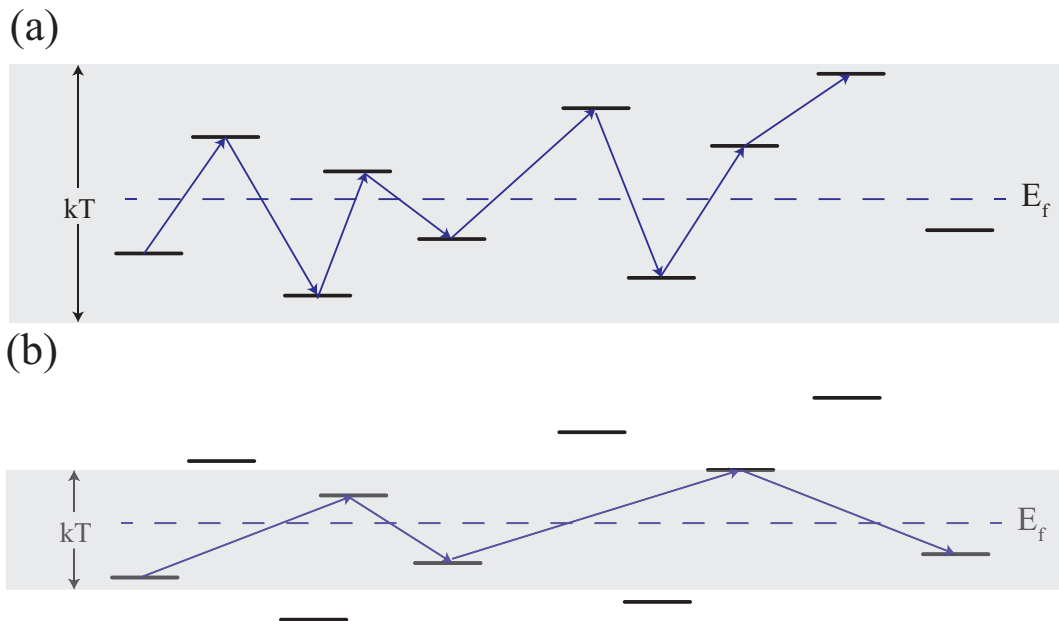


Figure 2.5: Schematic diagram showing Variable range hopping. When the temperature is low enough, jumping to further site is much easier than the nearest one. (a) and (b) are NNH and VRH model respectively.

In a highly disordered system, carriers are not delocalized and the strong localization of carriers occurs at a low enough temperature. This behavior is known as a strong localization. For example, in a doped semiconductor, carriers cannot acquire enough thermal energy $k_B T$ to be excited into the conducting band as the temperature decreases. The dominant transport mechanism is no longer Drude model but the hopping transport behavior.

Figure 2.5(a) shows the near neighbor hopping (NNH), which occurs at the high temperature regime. However, at the low temperature regime, impurities will induce some

localized state [2, 3] and transport to near localized sites is much more difficult than to remote sites. This is called the variable range hopping (VRH) as shown in figure 2.5(b). The dominant transport conductivity of these models can be written as an exponential term.

$$G(T) = G_0 \exp\left(-\frac{T_0}{T}\right)^p, \quad (2.13)$$

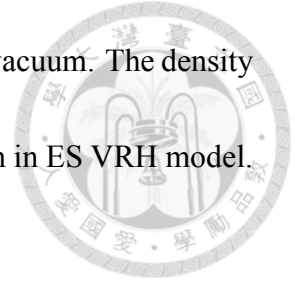
where G_0 is the prefactor, T_0 is the characteristic temperature, and p is the dominant exponent. At high temperature, NNH can be well described by Arrhenius-type thermal activation model, which $p = 1$ with $E_a = k_B T$. E_a is the activated energy. At lower temperature, carriers prefer hopping to remote sites and p is equal to $1/3$ in a two-dimensional system. Also, the hopping length ξ can be calculated through

$$k_B T_0 \equiv k_B T_M = \frac{13.8}{g_f \xi^2}, \quad (2.14)$$

where k_B is the Boltzmann constant, T_M is the characteristic temperature in the Mott VRH model, g_f is the density of states near the neutrality point, and ξ is the variable hopping length. This behavior is proposed by Mott in 1969 [4, 5]. In 1975, Efros and Shklovskii [6–8] propose that coulomb interaction is an important factor. In ES VRH model, p should be revised as $1/2$ and

$$K_B T_0 = \frac{6.2e^2}{4\pi\epsilon_r\epsilon_0\xi}, \quad (2.15)$$

where ϵ_r and ϵ_0 are the electric permittivity of the material and of the vacuum. The density of states g_f in equation 2.14 is suppressed by the Coulomb interaction in ES VRH model.





Bibliography

- [1] N. Ashcroft and N. Mermin, *Solid State Physics* (1976).
- [2] V. M. Pereira, F. Guinea, J. M. B. Lopes dos Santos, N. M. R. Peres, and A. H. Castro Neto, *Phys. Rev. Lett.* **96**, 036801 (2006).
- [3] F. Joucken, Y. Tison, J. Lagoute, J. Dumont, D. Cabosart, B. Zheng, V. Repain, C. Chacon, Y. Girard, A. R. Botello-Méndez, S. Rousset, R. Sporcken, J.-C. Charlier, and L. Henrard, *Phys. Rev. B* **85**, 161408 (2012).
- [4] N. Mott, *Philos. Mag.* **19**, 835 (1969).
- [5] C. Y. Cheah, C. Gómez-Navarro, L. C. Jaurigue, and A. B. Kaiser, *J. Phys.-Condens. Mat.* **25**, 465303 (2013).
- [6] B. I. Shklovskii, *Sov. Phys. Semicond.* **6**, 2335 (1972).
- [7] B. I. Shklovskii, *Sov. Phys. Semicond.* **6**, 1964 (1973).
- [8] A. L. Efros and B. I. Shklovskii, *J. Phys. C: Solid State Phys.* **8**, L49 (1975).



Chapter 3

Sample Fabrication

3.1 Graphene Transfer Technique

In this section, a common used transferred method for graphene films onto a desired substrate is introduced. Our CVD graphene sample was supported by Prof. Yang-Fang Chen and his research group, and the same technique was utilized in this thesis.

First, Polymethylmethacrylate (PMMA) is spin-coated onto the graphene as a support and the thin PMMA/graphene/Cu film are baked for 10 mins at 120 °C to solidify the PMMA. Put it on the surface of 1M iron nitrate (FeCl_3) solution for 10 mins to etch the bottom Cu foil. After removal of the Cu foil, we carefully rinse it in the deionized (DI) water. Then, it is transferred to the desired substrate. At last, the substrate is baked for 10 min at 90 °C, and then it's immersed into acetone solution for about 30 min to dissolve the PMMA layer. Finally, the sample with graphene on SiO_2/Si substrate is prepared for

the next photolithography process.



3.2 Hall-bar patterning

We use the photolithography method to pattern our sample into a Hall bar. It contains two main processes: the Hall bar patterning and the contact patterning.

In the Hall bar patterning, we used a spin coater to deposit a thin photoresistance film, AZ 1500, on our sample as shown in figure 3.1(b). The speed of the machine was fixed at 500 rpm for 5 s , 1000 rpm for 10 s, and then, 4000 rpm for 40 s in sequence. After the coating process, the sample was placed on a baker. The temperature of the baker was held at 100 °C for 1 min to enhance the viscosity of the photoresistance. The mask aligner was then utilized to expose our sample under the UV light for 80 s (the UV light intensity: 4.1 kJ/cm²s) followed by an immersion in tetramethylammonium hydroxide (TMAH) developer for 1 min. In the developing process, the unexposed region will be etched as shown in figure 3.1(e). Then, we used the reactive ion etching (RIE) to remove the unwanted graphene region with O₂ plasma at 40 sccm, power 60 W for 1 min. Finally, the sample was cleaned in the acetone solution to remove the photoresistance. At this time, the Hall bar pattern was finished and our sample was ready for the contact pattern process.

In the second process, Ti/Au contacts were deposited by the E-beam evaporator and

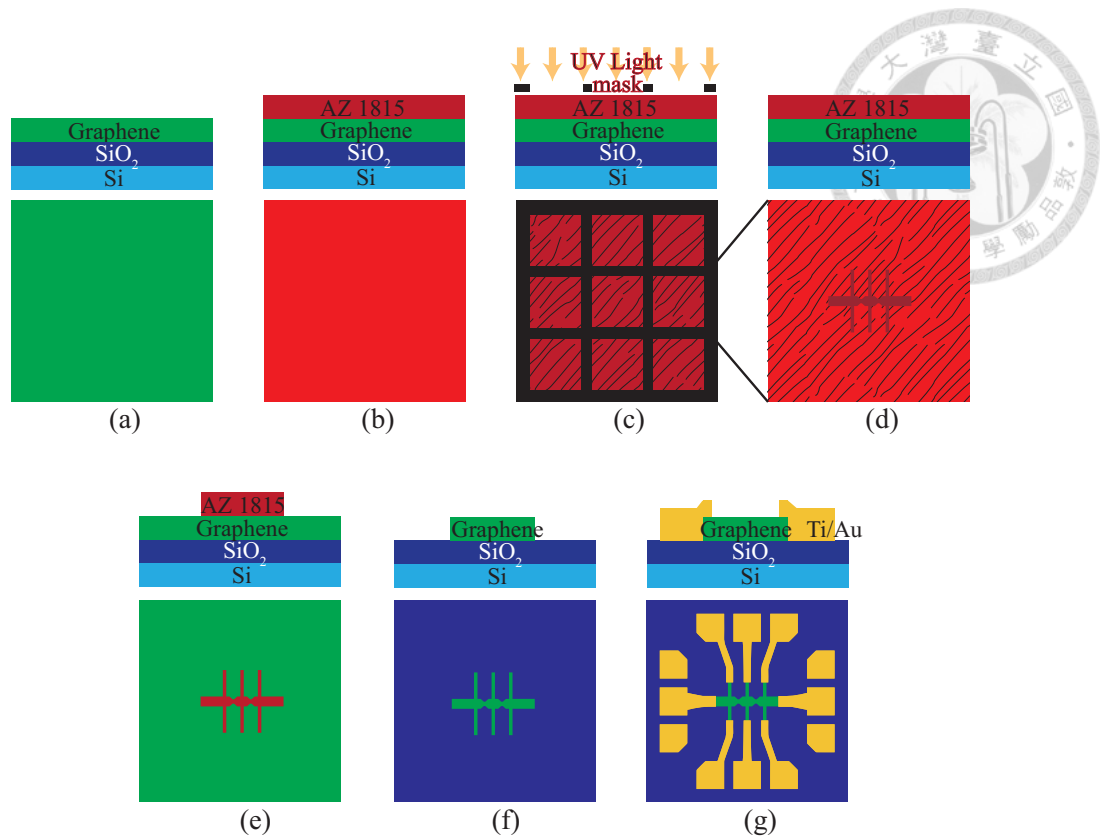


Figure 3.1: The cartoon diagram of our photolithography processes. (a)-(g) the top view and the side view of each process (a) At first, the graphene sample is transferred to the SiO₂/Si substrate. (b) The photoresistance is deposited on the sample via spin coating method. (c) The sample is exposed under the UV light with our optical mask. (e) the sample has been developed with the TMAH solution and etched by the O₂ plasma. (f) the final pattern of the hall bar (g) Au/Ti film is then deposited on it respectively.

fabricated through the lift-off process. The thicknesses of Ti and Au were 5 and 50 nm as shown in figure 3.1(g).

3.3 Sample packaging



In order to measure our sample in the cryofree system, to install our sample into a suitable package is necessary. We used a wire bonder to connect the pads on the package to the contacts on the sample. In addition, we used the silver colloid to directly connect the pad on the package to the metal plate, below the Si substrate to serve as the back gate. With this tunable back gate plate, ambipolar field effect could be observed in our sample. During the measurement, leakage current is not apparently observed (below 10^{-9} A). The package of our system and the final products is shown in figure 3.2.

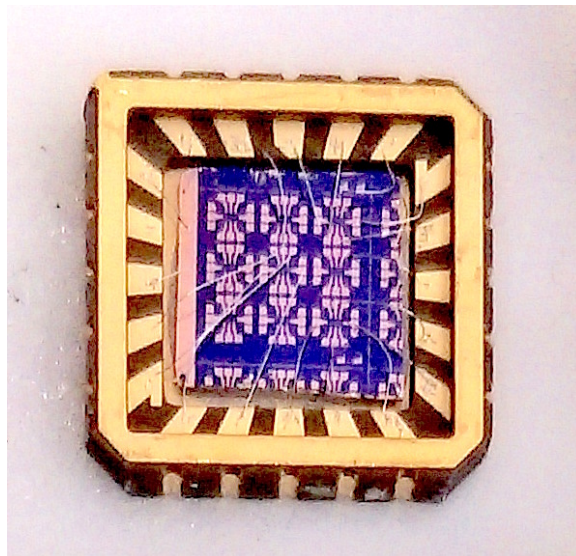


Figure 3.2: The top view of the sample and the system holder.



Chapter 4

Experimental Techniques

In this chapter, the experimental techniques used in data analysis are included. The mechanism of Raman spectroscopy, scanning electron microscopy, and cryogenic system are introduced in section 4.1, 4.2, and 4.3 in sequence. The four-terminal measurement setup is included in the last section.

4.1 Raman spectroscopy

Raman spectroscopy, named after Sir C. Raman, is a common spectroscopy used to discover the vibrational, rotational, and other low-frequency energy states. These kinds of energy states are unique for a certain material, so it provides the fingerprint of a material in a chemical analysis.

A light, or an electromagnetic (EM) wave, may be scattered if it impinge on an object.

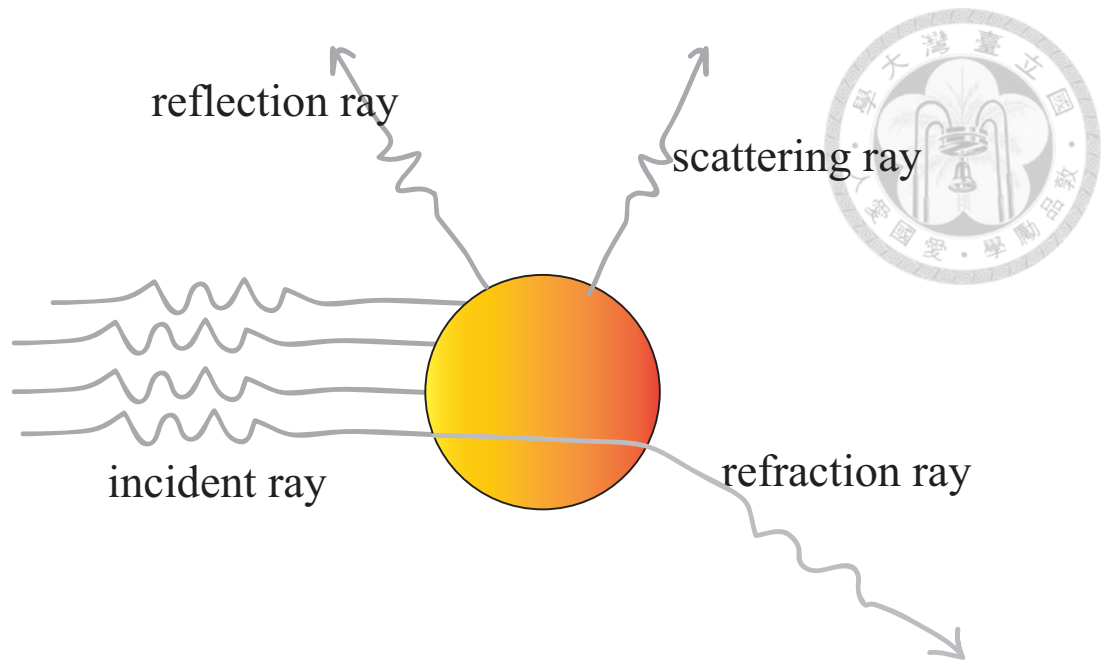


Figure 4.1: a schematic diagram of the light scattering process.

A common scattering process is shown in figure 4.1. The frequency of the outgoing light may or may not be the same to the incoming light. The process that an outgoing light has the same frequency as the incoming light is called the Rayleigh scattering. Otherwise, the one with lower (higher) frequency one is called Stokes (anti-Stokes) Raman scattering.

The physical mechanism of the Raman scattering will be described as follows.

As the incident EM wave is presented, dipole moments will be induced inside the material. The relation between the dipole moment, P , and the electric field E of the incident wave can be shown as

$$\vec{P} = \alpha \vec{E}, \quad (4.1)$$

where α is the polarizability of the material. The polarization of the electric field varies with time. Therefore, the polarization of the material also changes according to equation

4.1. It can be shown that

$$\vec{E} = \vec{E}_o \cos(2\pi\nu_o T) \quad (4.2)$$

and

$$\vec{P} = \vec{E}_o \cos(2\pi\nu_o T), \quad (4.3)$$

where ν_o is the frequency of the electric field ($\nu = c/\lambda$). α is related to the displacement of the charge ($\vec{p} = q\vec{D}$, where \vec{D} is the displacement and q is the electric charge), which is a small value. Thus, α can be written in the asymptotic form by using the Taylor expansion.

$$dD = D_o \cos(2\pi\nu_{vib} T) \quad (4.4)$$

and

$$\alpha = \alpha_o + \partial\alpha/\partial D dD, \quad (4.5)$$

where ν_{vib} is related to the lattice vibrational mode of the material, which is unique due to the variability of the band structure of the material. Substituting α in equation 4.1 by equation 4.5 and 4.4, we can rewrite the equation as

$$P = \alpha_o E_o \cos(2\pi\nu_o T) + \frac{\partial\alpha}{\partial D} D_o E_o \cos(2\pi\nu_o T) \cos(2\pi\nu_{vib} T) \quad (4.6)$$



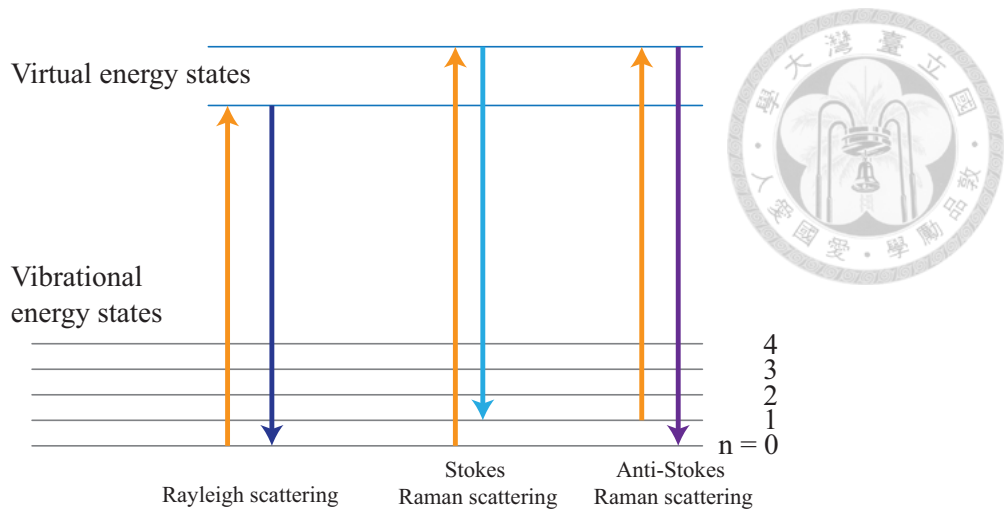


Figure 4.2: Illustration of Raman energy state for Rayleigh, Stokes, anti-Stokes Raman process. The electron will jump to the virtual state and then go back to the lower energy state coming with the emission light.

By using trigonometric identity, equation 4.6 can be written as

$$P = \alpha_o E_o \cos(2\pi\nu_o T) + \frac{\partial\alpha}{\partial D} \frac{D_o E_o}{2} \cos(2\pi(\nu_o + \nu_{vib})T) \cos(2\pi(\nu_o + \nu_{vib})T) \quad (4.7)$$

In equation 4.7, there are three domain frequencies of the induced dipole moment: ν_o , $\nu_o - \nu_{vib}$, and $\nu_o + \nu_{vib}$. The first one is the Rayleigh scattering, which is an elastic scattering process. The second and the third one are Stokes Raman and anti-Stokes Raman phenomena, which belong to the inelastic scattering process.

In the room temperature, the electrons prefer to stay in the lowest energy due to the Boltzmann distribution and are more likely to jump back to the lowest state. Thus, the intensity of Rayleigh scattering signal is much stronger than Stokes Raman scattering. Also, the signal of Stokes Raman scattering is much more obvious than anti-Stokes Raman

scattering.



4.2 Scanning electron microscopy

Scanning electron microscopy (SEM) is an useful instrument to scan the topography of the sample surface. Traditionally, an optical microscopy (OM) cannot resolve the image up to 500X due to the wavelength of the visible light. However, electron is used as the source of SEM to derive the image, and the wavelength of electron is much shorter than the visible light. Thus, the resolution of SEM can be naturally higher than the OM.

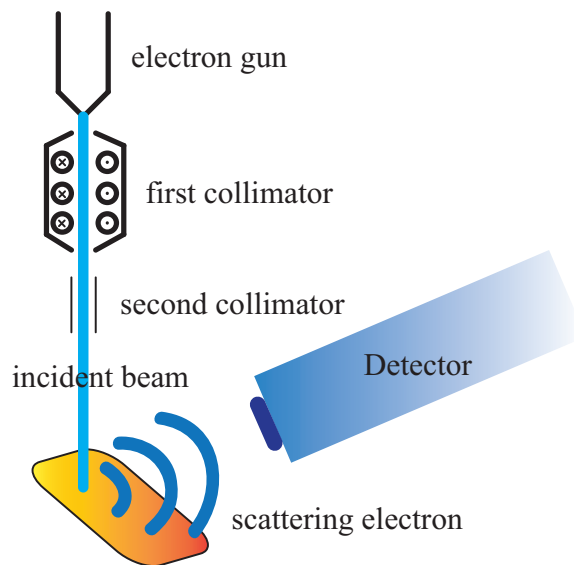


Figure 4.3: Schematic diagram of the SEM.

The schematic diagram of the SEM is shown in figure 4.2. An electron gun is used to inject the electrons with the magnetic field (first and secondary collimator) to align the electron beam. As the electrons approach the sample, the electron will interact with the orbital of the sample. Thus, electron scattering would occur, such as secondary electron

scattering, and back-scattering. A computer analysis is applied to resolve these data. Via these data, the image of the sample surface and other chemical properties of the sample can be derived from it.



4.3 Cryogenic system

In our experiment, we used the cryogen free dilution refrigerator manufactured by Oxford instrument to cool down our sample. We first put our sample on the MC plate, as shown in figure 4.4, and then we assembled the vacuum chamber.

The minimum temperature which the system can reach is about 13.6 mK. It contains two processes: pre-cooling stage and condensing stage. In the pre-cooling stage, Joule-Thomson cooling method is utilized. The system will vent a small amount of $^3\text{He}/^4\text{He}$ gas mixture through the pre-cooling loop (red circuit in figure 4.5). In the condensing stage, the mixture will be collected and go through another loop (see the green part in figure 4.5). According to the phase diagram of helium mixture(see figure 4.6), as the temperature is low enough, helium would be separated into two phases: the concentrated phase (practically 100% ^3He) and the dilute phase(about 6.6% ^3He and 93.4% ^4He). Therefore, as the machine pump liquid ^4He into the mixture, some of the ^3He must be evaporate to maintain the equilibrium. At last, due to the latent heat of ^3He , the system will be cooled down.

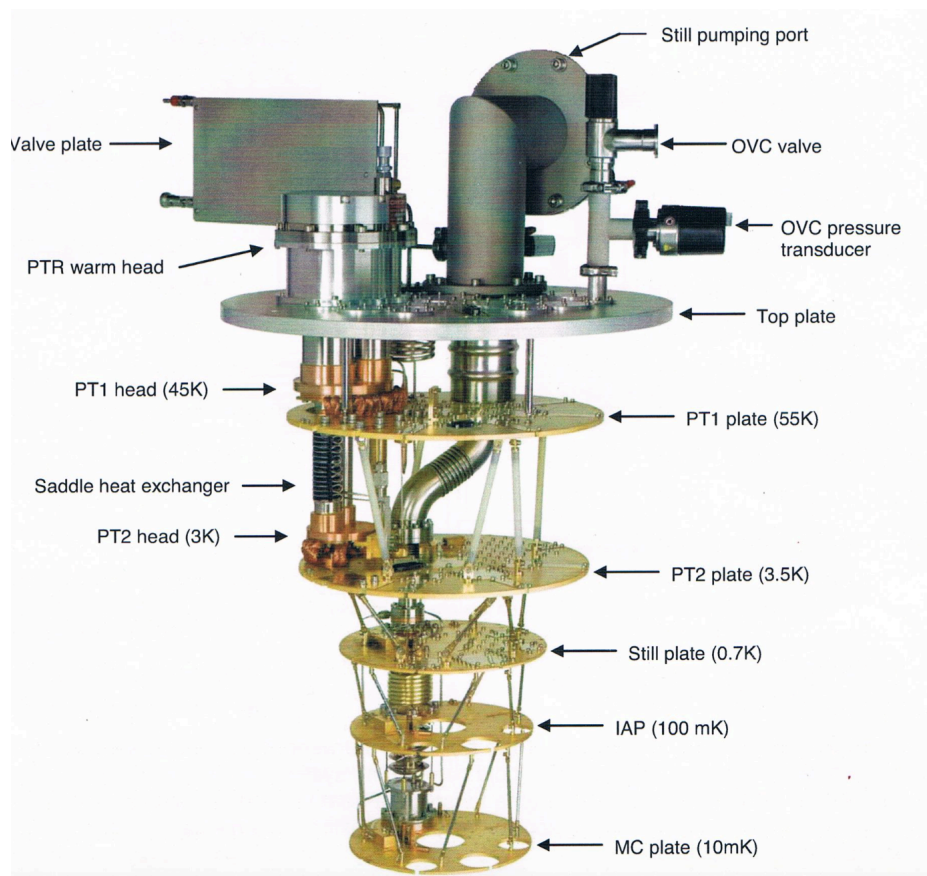


Figure 4.4: Side view of the Triton system.

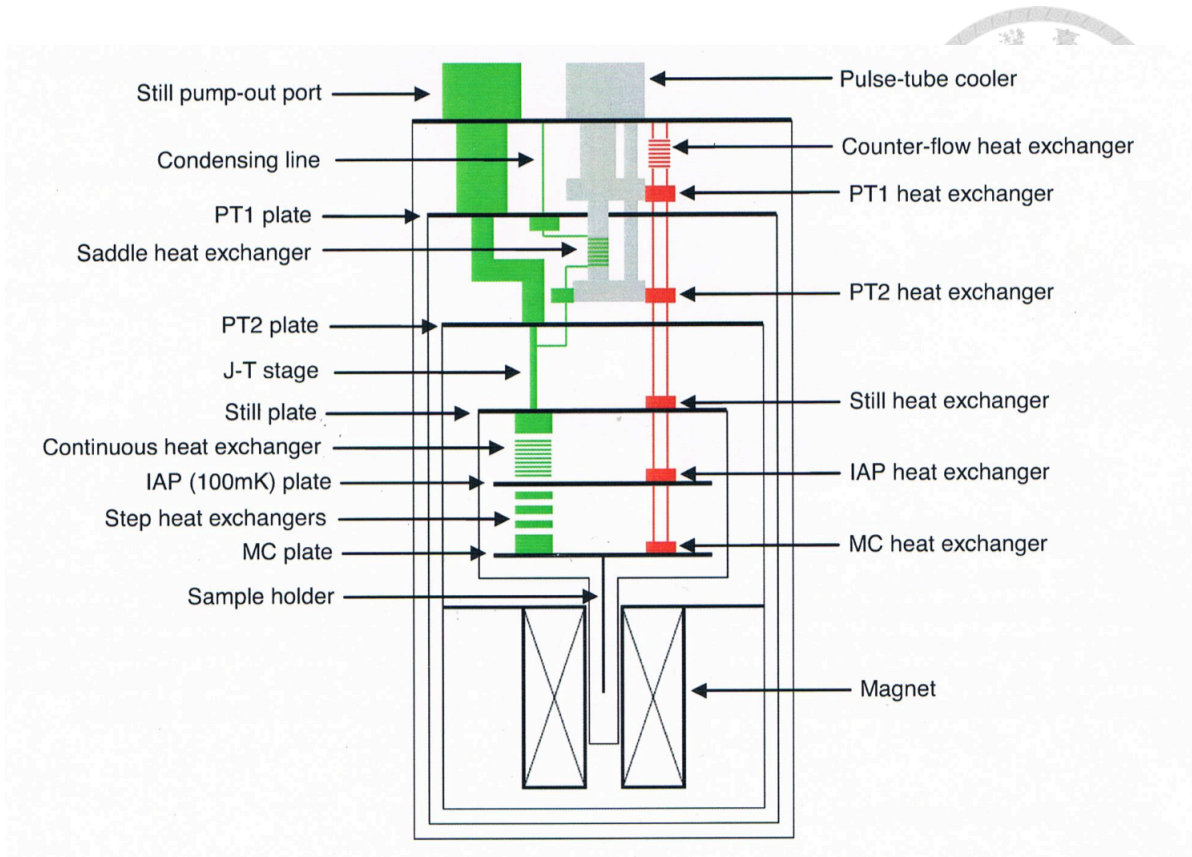


Figure 4.5: Schematic view of the system showing the main heat exchange mechanism. the pre-cooling circuit is shown in red and the dilution circuit in green.[1]

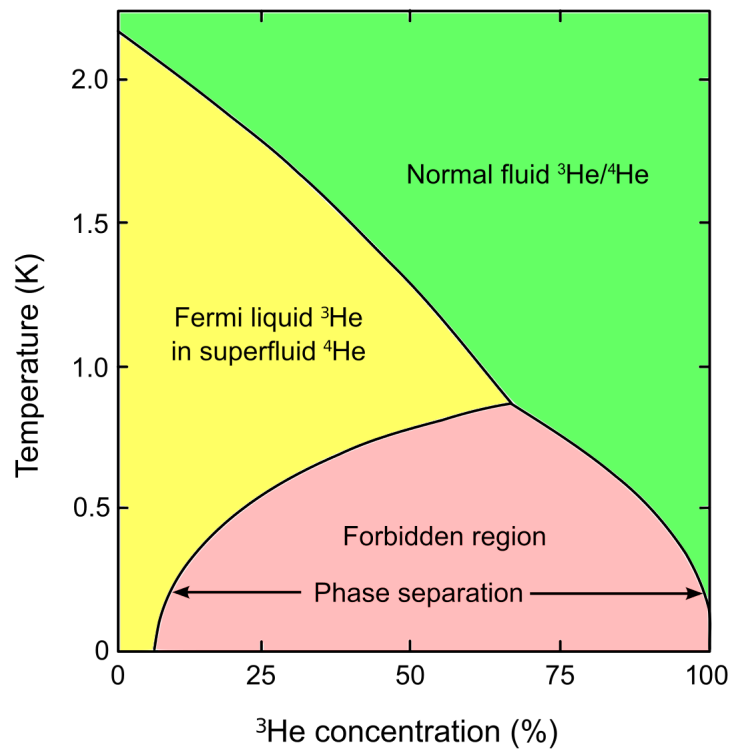


Figure 4.6: The phase diagram of $^3\text{He}/^4\text{He}$ phase diagram.[2]

4.4 Four-terminal resistance measurement



The four-terminal measurement is widely used in the cryogenic experiments due to its high accuracy. By separating the current source and the measurement unit from sharing the same contact, signals containing the contact resistance can be effectively reduced as compared to the traditional two-terminal measurement. According to van der Pauw method, this can reduce the inaccuracy resulted from the contact resistance.

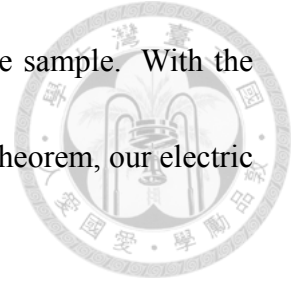
The van der Pauw method have these constriction: First, the shape of the sample must be flat and uniform; second, the sample cannot have any isolated holes; third, the sample should be homogeneous and isotropic; fourth, all four contacts must be located at the edges of the sample; fifth, the area of any individual contact should be at least an order of magnitude smaller than the area of the entire sample. Based on these constrictions, the resistance shown in figure 4.7 between M and N can be calculated as follows.

$$R_{mn,op} = \frac{V_{mn}}{I_{op}}, \quad (4.8)$$

where V_{mn} is the measured voltage across the point M and N, I_{op} is the current detected by the current source. By van der Pauw formula, the resistance defined by eq.4.8 will satisfy

$$e^{-\frac{\pi d R_{mn,op}}{\rho}} + e^{-\frac{\pi d R_{op,mn}}{\rho}} = 1, \quad (4.9)$$

where d is the thickness of the sample and ρ is the resistivity of the sample. With the help of four-terminal measurement, which satisfies the van der Paul theorem, our electric measurement can be much more accurate and efficient.



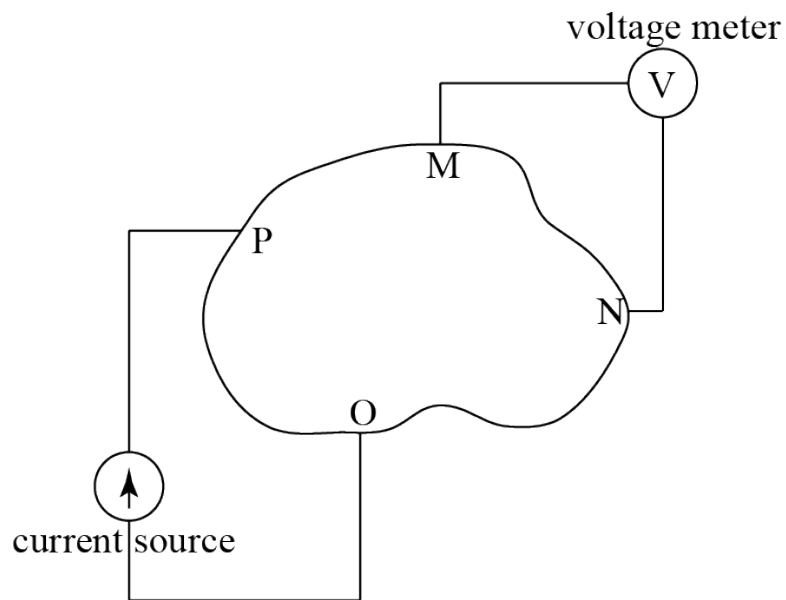


Figure 4.7: Illustration diagram of van der Pauw electrical configuration. The resistance $R_{mn,op}$ is defined as V_{mn}/I_{op} [3]



Bibliography

- [1] *Triton 200/400 cycrofree dilution refrigerator Operator's Handbook* (Oxford Instrument, 2012).

- [2] F. Pobell, *Matter and methods at low temperatures* (2007).

- [3] S. H. N. Lim, D. R. McKenzie, and M. M. M. Bilek, *Rev. Sci. Instru.* **80**, 075109 (2009).



Chapter 5

Transport through CVD-Grown

Graphene Constrictions

Many researches demonstrated that disorder and doping will lower the mobility of graphene nano-devices. These devices usually involved hydrogenated doping graphene [1, 2], nitrogen doping graphene [3], fluorinated doping graphene [4], devices of disorder from the substrate [5], and of the remaining photoresistance [6], etc. Hopping transport similar to those in reduced graphene oxide devices [7, 8] is pronounced in these kinds of disordered system. Hence, due to that thermal annealing was not applied to our samples before the measurement, chemical doping during each process may exist, such as nitrogen and oxygen adsorbed from atmosphere, substrate random disorder, or the photoresistance from the pattern process, etc. This allowed us to investigate in the low-mobility graphene

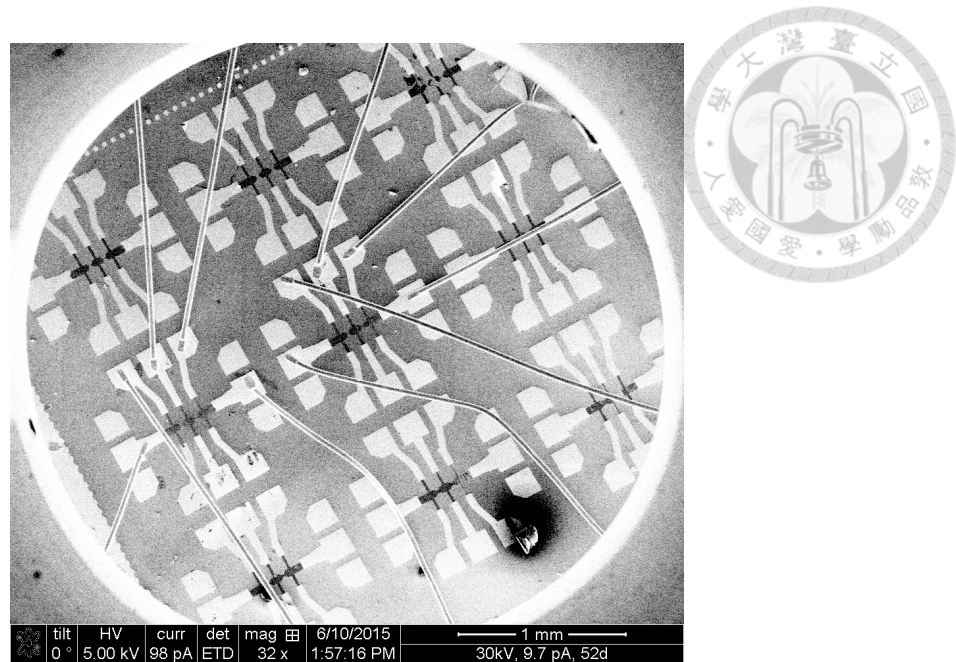


Figure 5.1: SEM picture of all the samples on a chip.

device and its transport behavior.

Our CVD graphene samples were provided by Prof. Yang-Fang Chen and his research group, which were fabricated via CVD method. Graphene was transferred to SiO₂ (300nm)/n+ Si substrate and then followed by the photolithography process as described in chapter 3. Si substrate was used as the back gate and SiO₂ layer was served as the dielectric material, where the capacitance of SiO₂ for 300 nm is around 11.6 nF/cm². There were three different channel widths on a single chip as shown in figure 5.1. The channel widths of each device were 1.25, 5.90, 25.09 μm respectively and the label of each device were device 1 (D1), device 2 (D2), device 3 (D3) in sequence. The mobility of our sample could be calculated by equation 2.12 and is 400 cm²/Vs at 2 K.

A Four-terminal measurement method was applied to scan the electrical properties of our sample with a Keithley 2400 General-Purpose Source meter served as the current

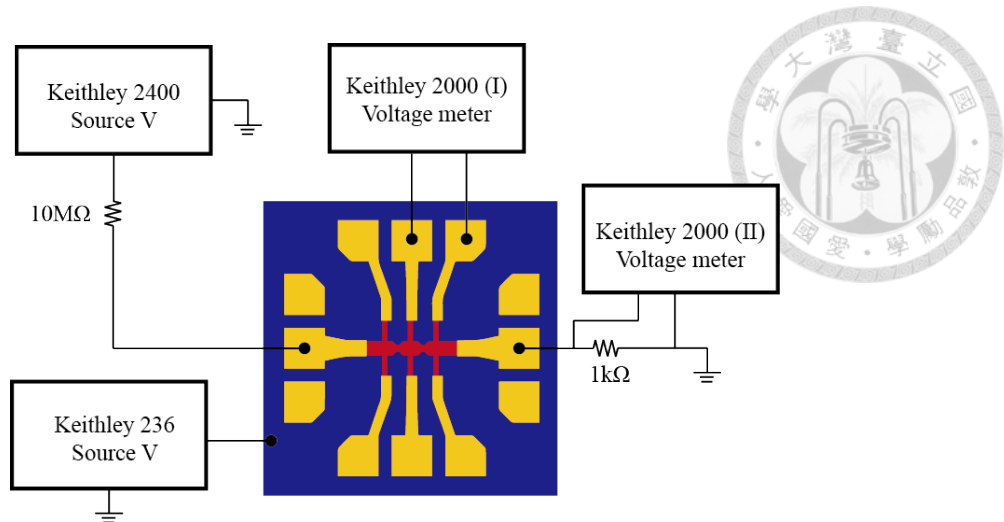


Figure 5.2: The configuration of the four-terminal measurement.

source and a Keithley 2000 Multimeter connected to the other two pads to measure the voltage difference. The back gate voltage is controlled by a Keithley 236 Source Measure Unit. Also, the sample was connected to a 1 K Ω resistance in series and another Keithley 2000 measured the voltage difference of this resistance as a current monitor. The setup of four-terminal measurement was ready and a LabVIEW program was used to control these machines. Following sections will show the electrical measurement of our samples under low temperature regime.

5.1 Ambipolar Field Effect and Nonlinear I - V Curves

Figure 5.5 gives an overview of the current-voltage (I - V) curve at different back gate voltage. By changing the gate voltage from -2.5V to 17.5V , Fermi level is tuned from the hole region to the neutrality point ($V_{BG} = 17.5\text{V}$). Thus, the slope of the I - V curve, which is the conductivity, becomes smaller as the back gate voltage approaches 17.5V . On the

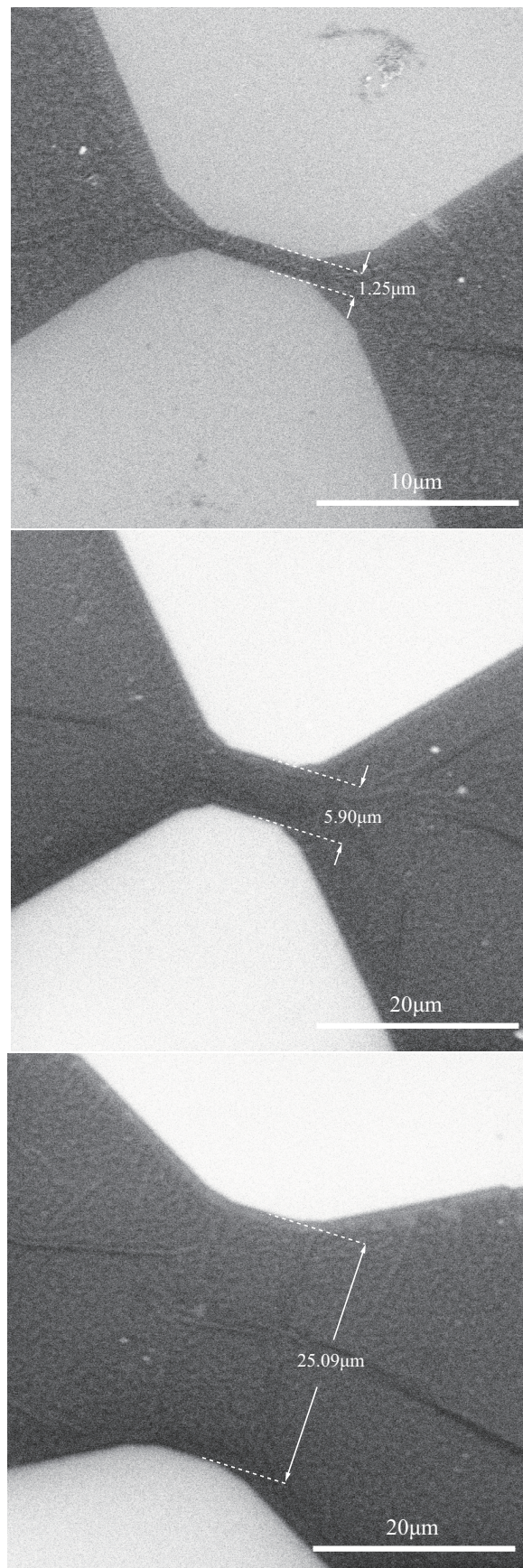


Figure 5.3: SEM picture of each device. From top to bottom are label as D1, D2, and D3 in sequence. The channel widths of each device are 1.25, 5.90, 25.09 μm respectively.

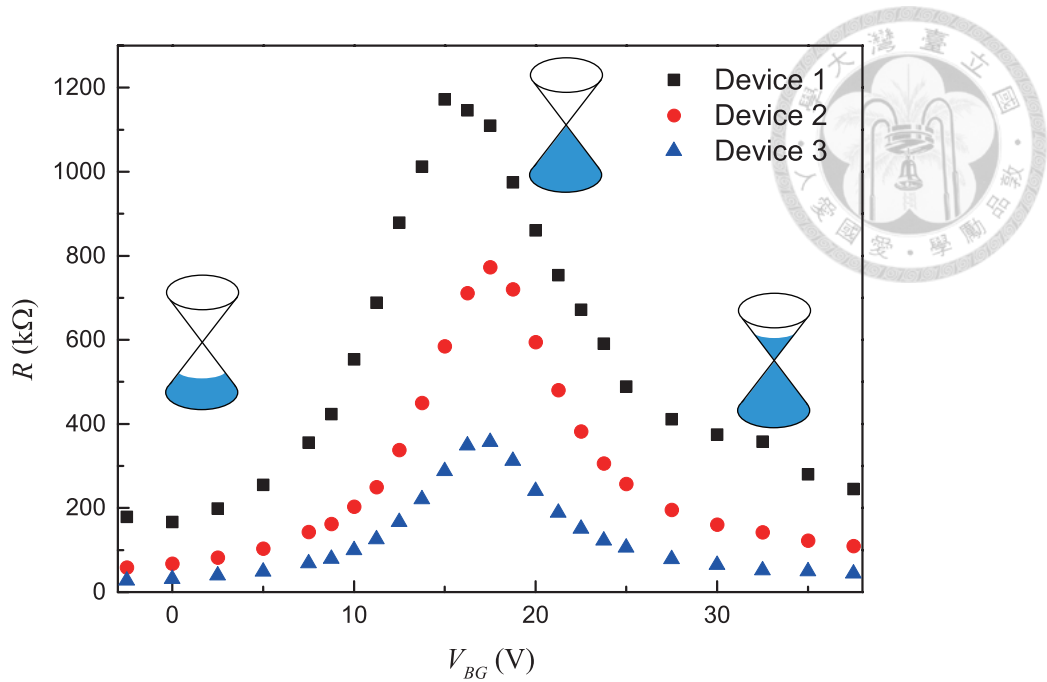


Figure 5.4: Resistivity R at low bias field versus V_{BG} , defined as dV/dI , at different back gate voltage. The Dirac point of three devices are around 17.5 V, which means that doping level is the same. At V_{BG} lower than 17.5 V is in hole region and on the otherside (higher than 17.5V) is in electron region.

other hands, as the back gate voltage increases, Fermi level is then tuned to the electron region and the slope increases as well. Figure 5.4 shows the resistance R , defined as dV/dI at the low field regime, varies with the back gate voltage. This figure reveals the properties of conical band structure in graphene and this is called the ambipolar field effect as depicted in other controllable-gate devices of graphene sample [4, 9–11].

As the temperature decreases, the I - V curve becomes more nonlinear at low-field region as shown in figure 5.7. The conductance, the slope in the figure, decreases as the temperature decreases, which exhibits an insulator behavior. D1 and D2 also show this nonlinear behavior and insulator behavior, and their I - V curves are included in appendix A.

I focus on this nonlinear behavior in this thesis.

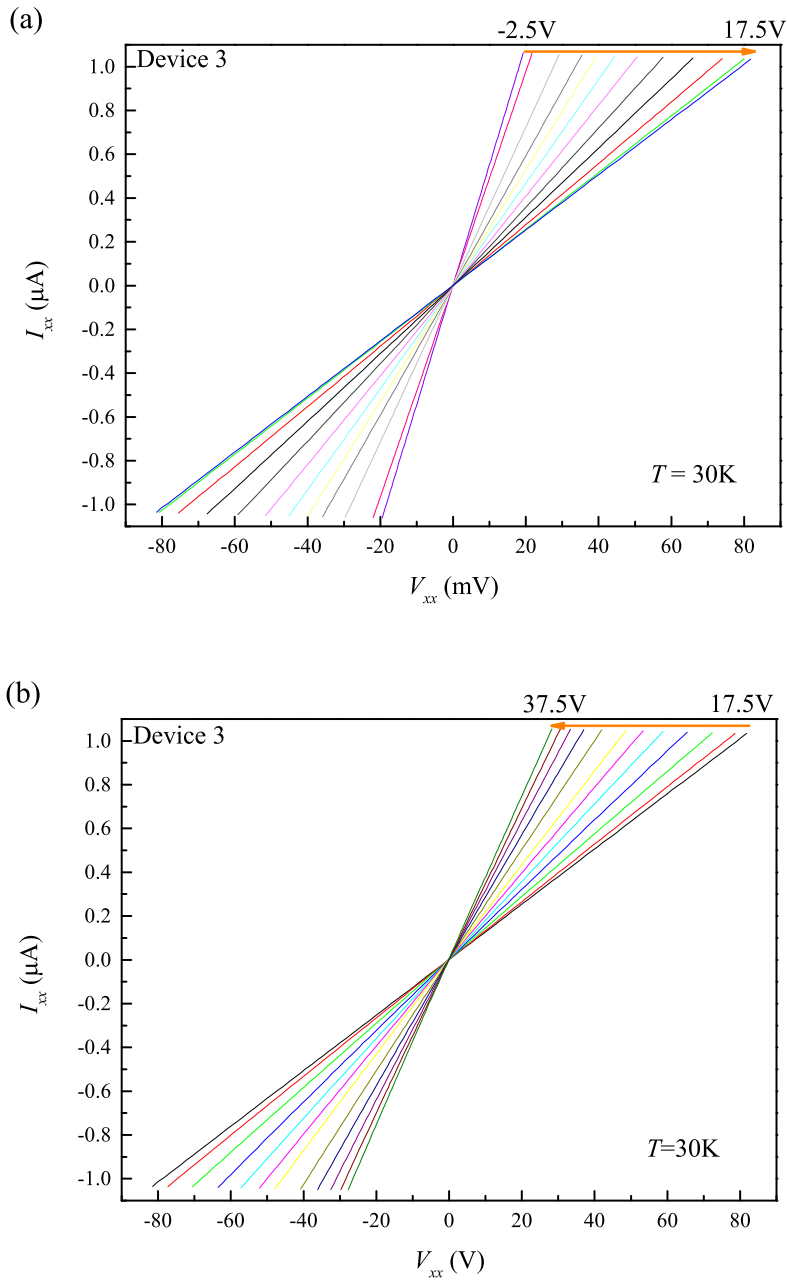


Figure 5.5: I - V curves for D3 at 30K. (a) and (b) are in the hole and the electron region respectively. The back gate voltage is set at $-2.5, 0, 2.5, 5, 7.5, 8.75, 10, 11.25, 12.5, 13.75, 15, 16.25, 17.5$ V from left to right for figure a; $17.5, 18.75, 20, 21.25, 22.5, 23.75, 25, 27.5, 30, 32.5, 35, 37.5$ V from right to left for figure b.

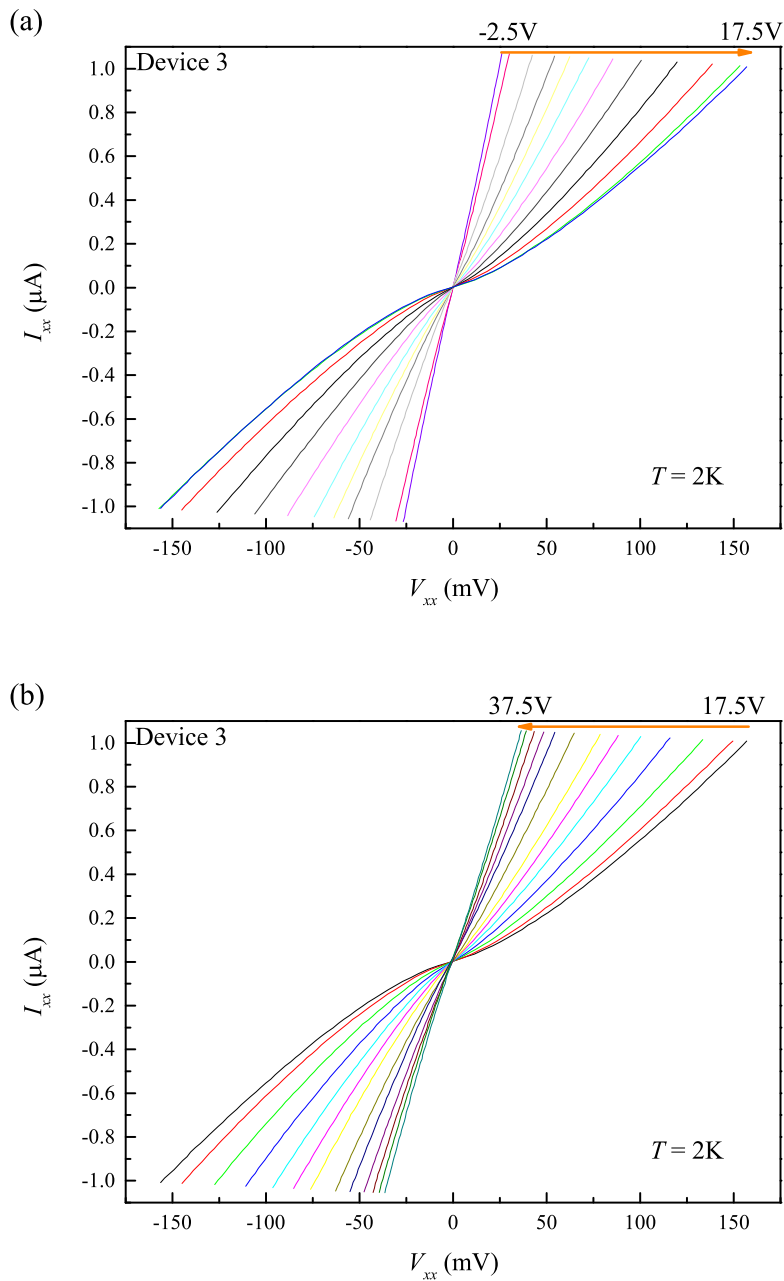


Figure 5.6: I - V curves for the D3 at 2 K. (a) and (b) are in the hole region and in the electron region respectively. The back gate voltage is set at $-2.5, 0, 2.5, 5, 7.5, 8.75, 10, 11.25, 12.5, 13.75, 15, 16.25, 17.5$ V from left to right for figure a; $17.5, 18.75, 20, 21.25, 22.5, 23.75, 25, 27.5, 30, 32.5, 35, 37.5$ V from right to left for figure b.

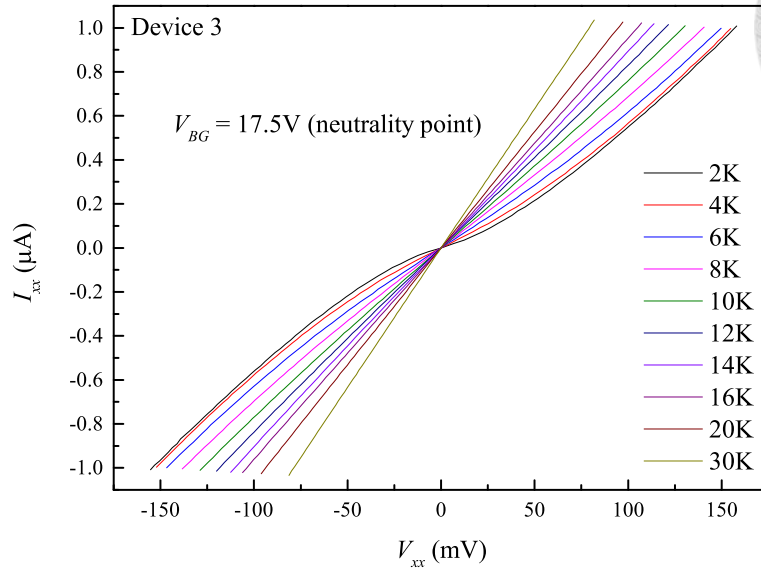


Figure 5.7: Temperature dependence of I - V curve at the neutrality point ($V_{BG} = 17.5$ V) for D3.

Figure 5.6 shows that the nonlinear behavior is strong at the neutrality point. Curves far from the neutrality point are much more linear. This phenomena has been observed in other researches[8] and as a solution the VRH model is used to explain it. In this graph, as the Fermi level is far from the neutrality point, the energy of the carriers is larger than the potential of the tray hole which induced by the impurities. Thus, carrier transport far from the neutrality point cannot be affected by the impurities.

5.2 VRH Model for Three Devices

Many researches have pointed out that the nonlinear behavior of I - V curve can be well described by the VRH model in a disordered graphene system[2, 7, 12–14]. It indicates that the conductance G , defined as $\frac{dI}{dV}$, will followed by $G = G_0 \exp[-(\frac{E_0}{E})^p]$. Thus, the

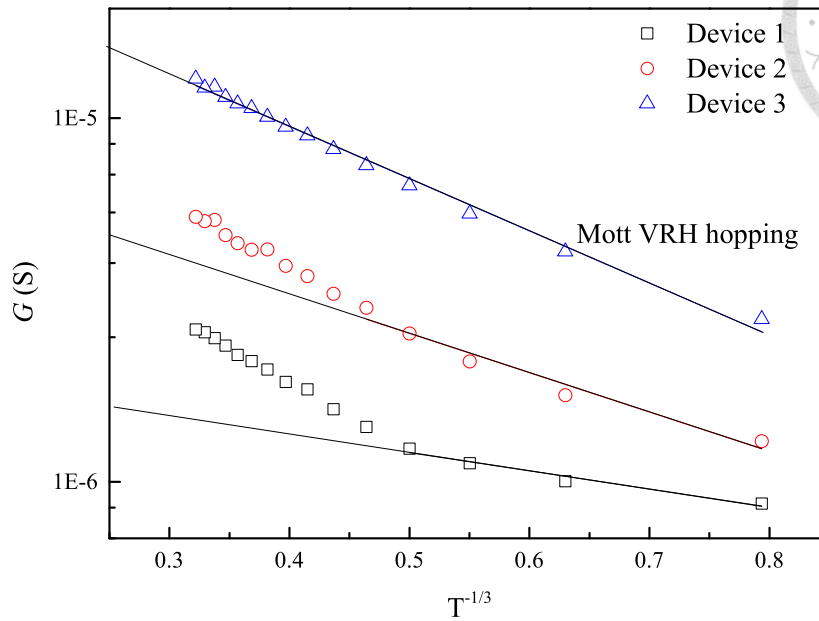


Figure 5.8: Semi-log plot of the conductance versus the temperature. The linear fitting method is applied to three devices in view of the VRH model.

conductance versus temperature is plotted in the semi-log scale so that this phenomenon can be better recognized. Figure 5.8 shows the temperature dependence for three devices.

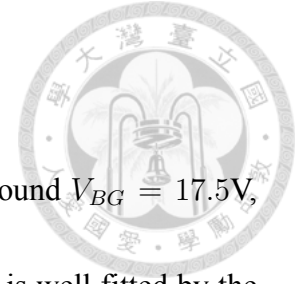
The $T^{-\frac{1}{3}}$ dependence is shown in this figure. Other forms of temperature dependence such as T^{-1} and $T^{-\frac{1}{2}}$ are also calculated, and the results are presented in the appendix B.

Among these temperature dependences, one third temperature dependence shows the best.

Thus, our samples can be well described by the Mott VRH model rather than the Efros-Shklovskii (ES) VRH model. This indicates that the coulomb interaction [7] is not significant in our samples.

Also, D3 can be well described by the Mott VRH model and the other two devices (D1 and D2) are not. D1 and D2 do not obey the VRH model at high temperature region (10 K to 30 K), but well described at low temperature (2 K to 8 K).

5.3 Inhomogeneous Impurities Effect



In figure 5.4, the resistance R of each device has a minimum around $V_{BG} = 17.5\text{V}$, representing that the doping level is almost the same. However, D3 is well fitted by the VRH model, which indicates that carrier transport is effectively much easier in D1 and that D3 is the hardest one. Thus, Raman spectroscopy was utilized to measure the strength of disorder. Many researches focused on this technique to detect the bonding type of graphene [15, 16]. Via Raman spectroscopy, the bonding strength for sp^2 and sp^3 orbital are related to the intensity of the Lorentz-shaped signal around 1350 and 1600 cm^{-1} , which are called G and D peak respectively. By dividing the intensity of these two peak, the strength of disorder can be observed.

Table 5.1 shows the ratio of I_D/I_G for the position along the bridge. The position of each point is shown in figure 5.9 and the original data of Raman shift signal is attached in the appendix C. The standard deviation of position 2 to 5 are calculated and shown in the lowest row. It becomes larger as the width of devices becomes much narrower. This represents that the inhomogeneity of impurities is much anomalous in the narrowest sample (D1).

This result is a bit surprising. Traditionally, as the disorder gets stronger, the conductivity would be smaller and the device would be more suitably described by the VRH model. Inferred from figure 5.4, the doping level is the same and the main difference is

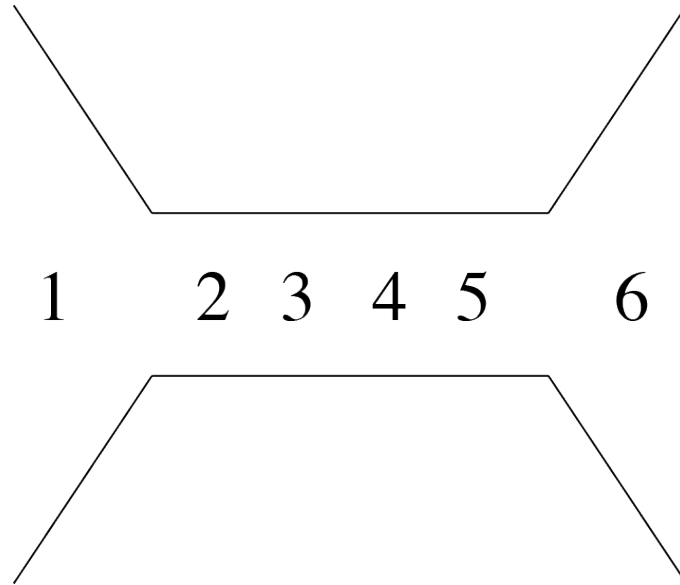
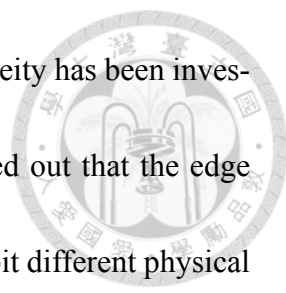


Figure 5.9: Schematic diagram of the position of Raman signal.

Table 5.1: Collected data for the strength of disorder, defined as I_D/I_G , at each position. Original Raman data are attached in the appendix C.

Region	Device 1	Device 2	Device 3
1	1.95	1.32	1.82
2	0.49	0.93	0.80
3	2.58	1.42	1.65
4	0.52	2.26	1.15
5	1.39	0.78	1.12
6	1.08	1.45	1.08
<i>Standard Deviation of 2 - 5</i>	<i>0.98</i>	<i>0.66</i>	<i>0.35</i>



the inhomogeneity of each device from Raman data. This inhomogeneity has been investigated in graphene nano-device. V. Panchal *et al* [17] have pointed out that the edge region on the graphene sheet (about $100nm$ from the edge) will exhibit different physical properties relative to the bulk region. Also, other experiments and simulations have been performed and proposed in last decade. All of these examined the edge effect such as the variation of mobility [18], inversed n-p type near neutrality point [17, 19], and irregular conducting profile [20], etc. Thus, in our devices, the channel width down to $1.25 \mu m$, the edge region (about $100 nm$ from each side) would take a great part on conducting behavior. Moreover, RIE method is applied to our etching process, which has been reported that the extra doping will exist [17]. All in all, as the channel width becomes narrower, the influence on the conducting channel becomes more pronounced. As a consequence, the positive influence of the conductivity of our sample to its inhomogeneity will be discussed in the next paragraph.

The induced band tails and the opening gap is almost the same in figure 5.10(a). However, with the help of inhomogeneity, the number of impurities-induced band tails and the opened band gap may vary with positions as shown in figure 5.10(b). In the latter case, carriers are much easier to transport than the former ones due to the inhomogeneity. The carriers have more conducting ways such as from the band tail to the near cone or from tails to tails. We suggest that this is the reason that D3 can be suitably described by the VRH model but D1 and D2 cannot.

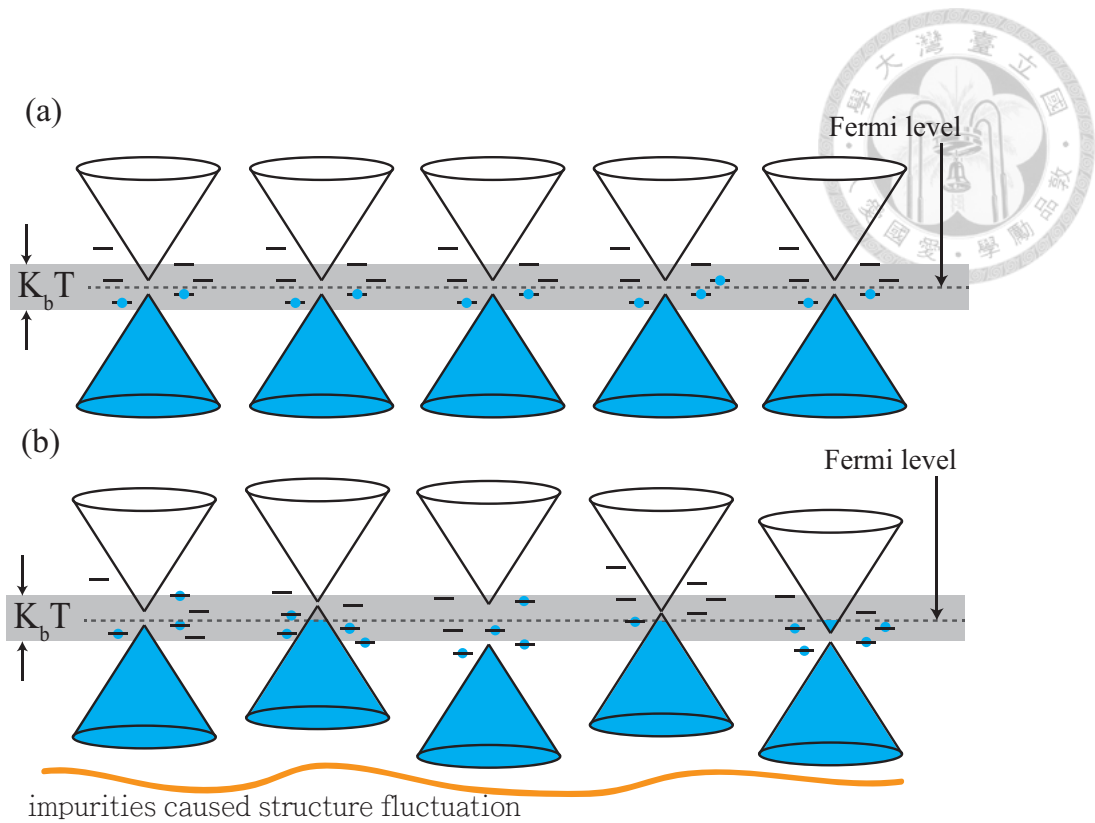


Figure 5.10: Cartoon diagram showing that the impact of impurities on the band structure of graphene. (a) and (b) are for the homogeneity and inhomogeneity cases respectively. Because D1 is much more inhomogeneous than D3, D1 and D3 are related to case b and a respectively.

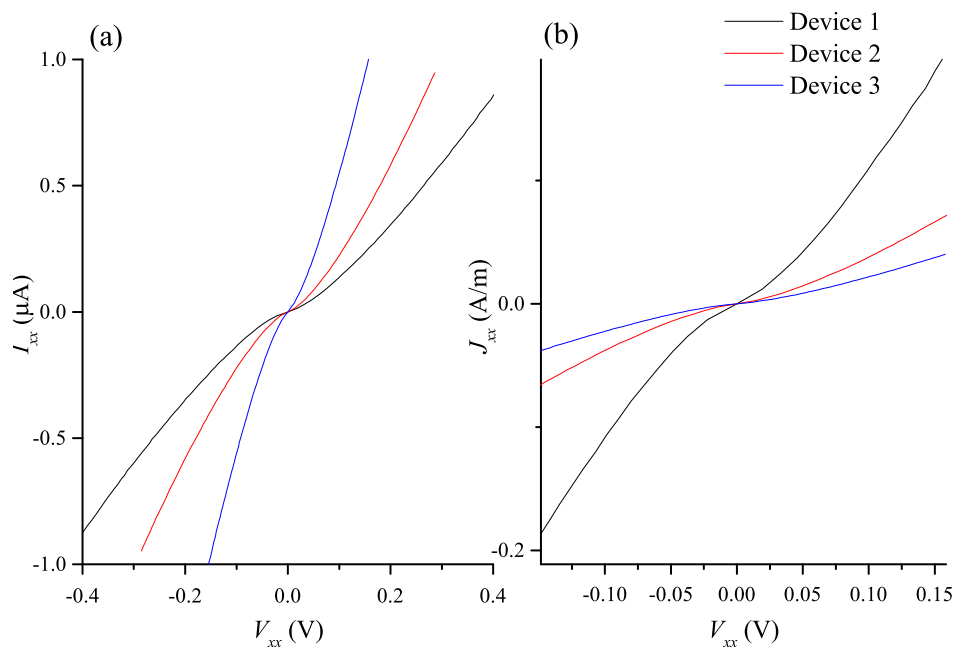
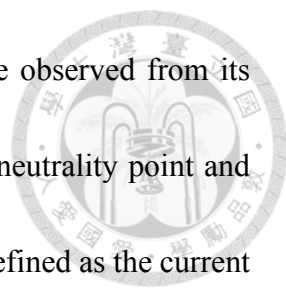


Figure 5.11: I - V curve and J - V curve for each device at the neutrality point.



The evidence of a better conducting transport in D1 can also be observed from its electrical measurement. Figure 5.11(a) shows the I - V curve at the neutrality point and figure 5.11(b) shows the J - V curves where J is the current density, defined as the current divided by the width of the channel $\frac{I}{W}$. In this figure, the current density in D1 is obviously larger than D2 and D3, representing that the effective conducting transport is much easier in D1. D3 exhibits low conducting transport. This result agrees well with the conclusion drawn from Raman analysis. These data support our model in figure 5.10. Both turn out that the impurities-induced inhomogeneous disorder will improve the carrier transport.

5.4 Transport Gap and Transition from Intermediated to High-Field Expression

With the adoption of the VRH model, we fit the conductance G versus temperature T to the power of $1/3$ with an appropriate range for D3. The characteristic temperature T_m , which is defined in the VRH model $G(T) = G_p \exp[-(\frac{T_m}{T})^{-1/3}]$, is plotted at each back gate voltage V_{BG} in figure 5.12. An offset to the x-axis has been added, which shift the Dirac point to zero x-axis. Due to the fact that the effective barrier height is equal to $\langle E_b \rangle = \langle E_b^0 - (E_F - E_{Dirac}) \rangle$ [21], it will have a maximum at Dirac point and decreases as $E_F - E_{Dirac}$ increases. Thus, the corresponding characteristic temperature T_m will have a maximum value at the neutrality point. Moreover, the transport gap can be derived

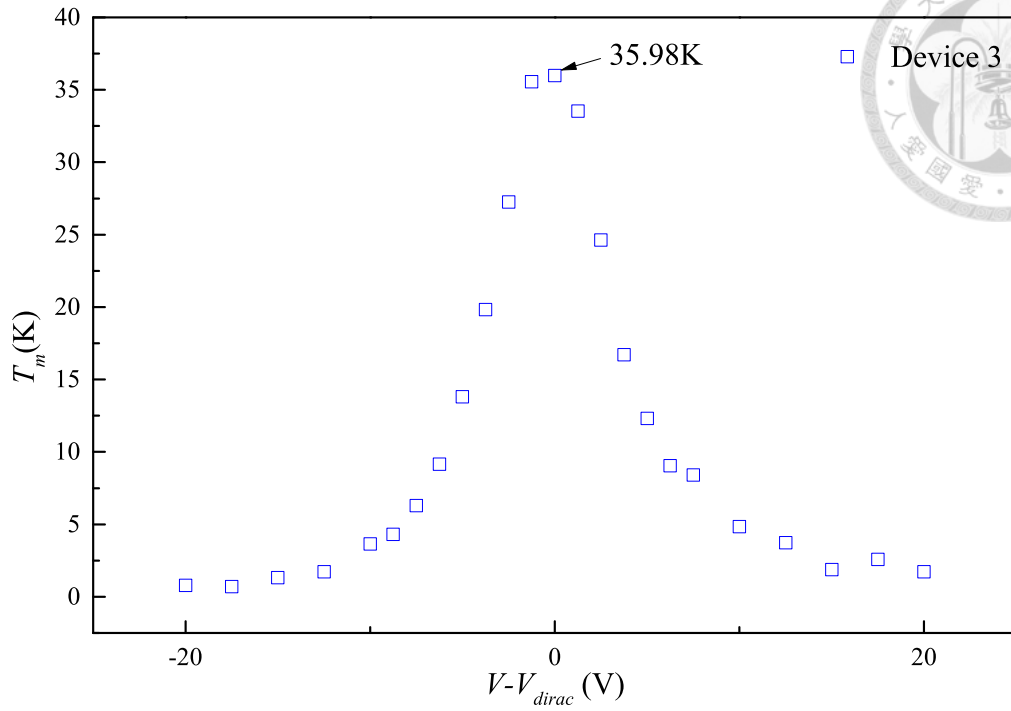


Figure 5.12: Characteristic temperature T_m versus voltage relative to Dirac point $V - V_{Dirac}$ for D3.

as follows. The density of the state is estimated as $g_f \approx 10^{18} \text{ eV}^{-1}\text{cm}^{-3}$, which is a typical value for an amorphous carbon film. Therefore, the mean hopping distance can be calculated through equation 2.14: $\xi = \sqrt{\frac{13.8}{k_b T_m g_f}} = 67 \text{ nm}$ and the transport gap [2, 22] can be derived via $E_G \approx \hbar V_F / \xi = 1.0 \text{ meV}$, which is considerably lower than those discovered in rGO, graphene nanotube, and so on. Via using the VRH model, the transport gap opened by the existence of induced impurities is once again proved by our devices.

Following by the work of CY Cheah *et al* [8], a crossover from intermediated-field dependent to high-field dependent VRH hopping may possibly be observed in a partially disordered graphene system. Three kinds of scenarios have been described by Mott[23], Pollak-Riess [24], and Shhklovski [25, 26] equation. These equations describe the con-

ductance at low-field, intermediate, and high-field regime respectively and are shown in equation 5.1 in sequence.



$$G(T) = G_0 \exp\left(-\frac{T_0}{T}\right)^p \quad (5.1a)$$

$$G(T, E) = G_1 \exp\left(-\frac{T_0}{T}\right)^p \exp\left(\frac{E}{E_a}\right) \quad (5.1b)$$

$$G(E) = G_2 \exp\left(-\frac{E_0}{E}\right)^p \quad (5.1c)$$

where G_0 , G_1 , G_2 are the prefactors for each expression, p is the exponent related to the dimension of the system ($p = 1/3$ for 2D system), T_0 and E_a are the characteristic temperature and the activation energy.

The transition between each equation at a given temperature can be recognized as follows. As the electric field decreases from high-field limit, the conductance in equation 5.1(c) decreases at a faster rate than equation 5.1(b). Thus, Pollak-Ries equation will dominate the conducting behavior. Moreover, as the electric field decreases further, the temperature term ($\exp(-\frac{T_0}{T})^p$) will over-press the electric field term ($\exp(\frac{E}{E_a})$). Thus, the conductance will wholly driven by the temperature term and goes into Mott expression.

For our devices, D3 is well fitted by the VRH model at low-bias electric field. By plotting the conductance G , defined as V/I here, the transition from the intermediate-field expression to the high-field expression can be will recognized. Figure 5.13 shows that $\ln G$

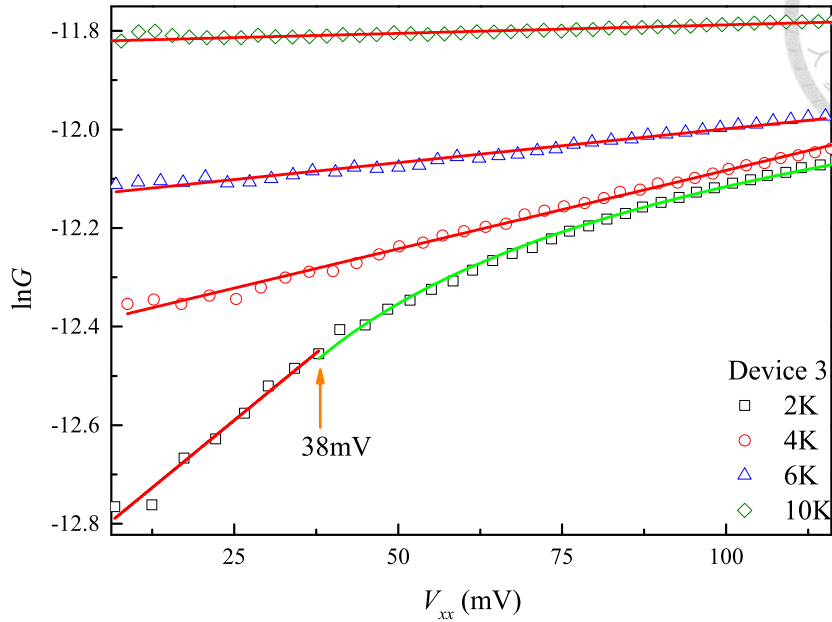
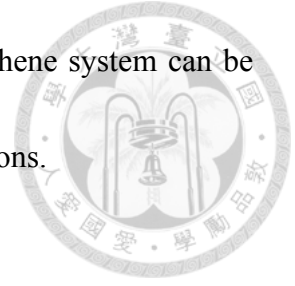


Figure 5.13: $\ln G$ versus V_{xx} at different temperature for D3. The red and green lines in the diagram are the fitting curve for Pollak-Riess and Shklovskii expression respectively.

increases linearly with V_{xx} , which follows the Pollak-Riess expression (equation 5.1(b)) at the high temperature region. However, as the temperature is decreased to 2 K, the dependence between $\ln G$ and V_{xx} is no longer correct. It follows the Shklovskii's high field expression (equation 5.1 (c)), instead. Since the crossover from two expressions is smooth, the slopes at the cross-section point should be the same. This gives out the turning electric field $E_c(T) = (pE_a E_0^p)^{1/p+1} = (E_a E_0^{1/3}/3)^{3/4}$ ($p = 1/3$ expression). Noted that the distance between two electrodes is $98.7\mu\text{m}$ and E_a and E_0 are 927.3 Vm^{-1} and 773.7 Vm^{-1} respectively, which are derived from the fitting parameter of the curve at 2 K. With these physical parameters, the crossover voltage is 0.038 V as shown in the figure.

In D3, a smooth crossover from Rollak-Riess to Shklobskii VRH is observed. Namely,

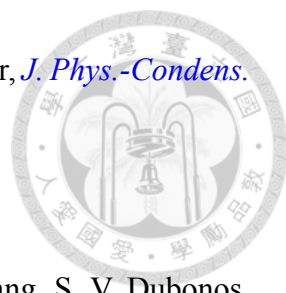
the behavior of carrier transport in a homogeneous disordered graphene system can be thoroughly described by Mott, Pollak-Riess, and Shklovskii expressions.






Bibliography

- [1] C. Chuang, R. Puddy, H. D. Lin, S. T. Lo, T. M. Chen, C. Smith, and C.-T. Liang, *Solid State Commun.* **152**, 905 (2012).
- [2] S.-T. Lo, C. Chuang, R. K. Puddy, T.-M. Chen, C.-G. Smith, and C.-T. Liang, *Nanotechnology* **24**, 165201 (2013).
- [3] Y. F. Lu, S. T. Lo, J. C. Lin, W. Zhang, J. Y. Lu, F. H. Liu, C. M. Tseng, Y.-H. Lee, C.-T. Liang, and L.-J. Li, *Nano Lett.* **7**, 6522 (2013).
- [4] F. Withers, M. Dubois, and A. K. Savchenko, *Phys. Rev. B* **82**, 073403 (2010).
- [5] R. A. Nistor, M. A. Kuroda, A. A. Maarouf, and G. J. Martyna, *Phys. Rev. B* **86**, 041409 (2012).
- [6] K. Kumar, Y.-S. Kim, and E.-H. Yang, *Carbon* **65**, 35 (2013).
- [7] D. Joungand and S. I. Khondaker, *Phys. Rev. B* **86**, 235423 (2012).

- 
- [8] C. Y. Cheah, C. Gómez-Navarro, L. C. Jaurigue, and A. B. Kaiser, *J. Phys.-Condens. Mat.* **25**, 465303 (2013).
- [9] K. S. Novoselov, A. K. Geim, S. V. Morozov, D. Jiang, Y. Zhang, S. V. Dubonos, I. V. Grigorieva, and A. A. Firsov, *Science* **306**, 666 (2004).
- [10] J. Bai, R. Cheng, F. Xiu, L. Liao, M. Wang, A. A. Shailos, K. L. Wang, Y. Huang, and X. F. Duan, *Nat. Nano.* **5**, 655 (2010).
- [11] F. Amet, J. R. Williams, K. Watanabe, T. Taniguchi, and D. Goldhaber-Gordon, *Phys. Rev. Lett.* **110**, 216601 (2013).
- [12] M. Y. Han, Y. C. Brant, and P. Kim, *Phys. Rev. Lett.* **104**, 056801 (2010).
- [13] D. Joung, L. Zhai, and S. I. Khondaker, *Phys. Rev. B* **83**, 115323 (2011).
- [14] A. Pachoud, M. Jaiswal, Y. Wang, B.-H. Hong, J.-H. Ahn, K. P. Loh, and B. Özyilmaz, *Sci. Rep.* **3** (2013).
- [15] L. G. Cançado, A. Jorio, E. H. M. Ferreira, F. Stavale, C. A. Achete, R. B. Capaz, M. V. O. Moutinho, A. Lombardo, T. S. Kulmala, and A. C. Ferrari, *Nano Lett.* **11**, 3190 (2011).
- [16] A. Eckmann, A. Felten, A. Mishchenko, L. Britnell, R. Krupke, K. S. Novoselov, and C. Casiraghi, *Nano Lett.* **12**, 3925 (2012).

- 
- [17] V. Panchal, A. Lartsev, A. Manzin, R. Yakimova, A. Tzalenchuk, and O. Kazakova, *Sci. Rep.* **4** (2014).
- [18] M. Poljak, M. Wang, E. B. Song, T. Suligoj, and K. L. Wang, *Solid-State Electron.* **84**, 103 (2013).
- [19] E. J. H. Lee, K. Balasubramanian, R. T. Weitz, M. Burghard, K. Burghard, and K. Kern, *Nat. Nano.* **3**, 466 (2008).
- [20] A. Cresti and S. Roche, *New J. Phys.* **11**, 095004 (2009).
- [21] S.-T. Lo, O. Klochan, C.-H. Liu, W.-H. Wang, A. R. Hamilton, and C.-T. Liang, *Nanotechnology* **25**, 375201 (2014).
- [22] W. Y. Jang, N. N. Kulkarni, C. K. Shih, and Z. Yao, *Appl. Phys. Lett.* **84**, 1177 (2004).
- [23] N. Mott, *Philos. Mag.* **19**, 835 (1969).
- [24] M. Pollak and I. Riess, *Phys. C: Solid State Phys.* **9**, 2339 (1976).
- [25] B. I. Shklovskii, *Sov. Phys. Semicond.* **6**, 2335 (1972).
- [26] B. I. Shklovskii, *Sov. Phys. Semicond.* **6**, 1964 (1973).



Chapter 6

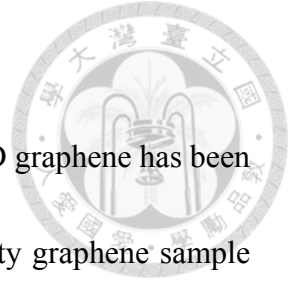
Conclusion

In this thesis, multi-width CVD graphene devices are realized through standard photolithography method. The nonlinear behaviors at the low temperature region are measured. Due to the disorder doped from the fabricating process, the band structure is no longer zero-band gap. Through analyzing via the VRH model, the transport gap is 1.00 meV for our device. This points out that disorders can open the band gap.

For three different channel width of graphene devices, doping level is the same among all devices (the same shift of Dirac point for three device) but the current density in D1 and D2 , which is much more narrow than D3, is instead higher than D3. With the help of the standard deviation for the disorder strength, the inhomogeneity is strong in D1 and weak in D3. Owing to the inhomogeneity, the number of inducing band tails and the energy gap between conducting and valence band would vary with positions. The conducting

channel, instead, would become better.

In our work, the width induced inhomogeneity in disordered CVD graphene has been investigated. In the future work, multi-width device in high mobility graphene sample can be done. We expect some other intrinsic properties such as the grain boundary in CVD graphene would affect the transport properties. Also, transportation under a vertical magnetic field may be influenced by the channel width.





Appendix A

Nonlinear I-V Curve for each Device

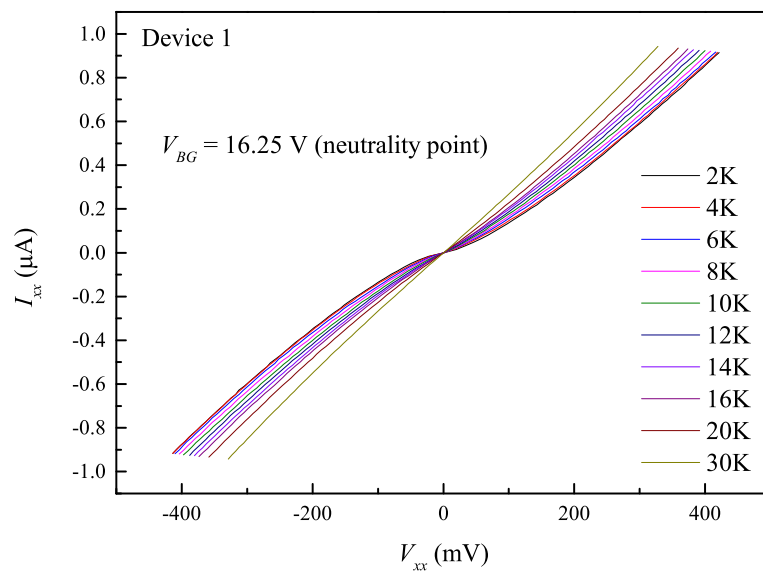


Figure A.1: Temperature dependence for D1 at the neutrality point ($V_{BG} = 16.25$ V).

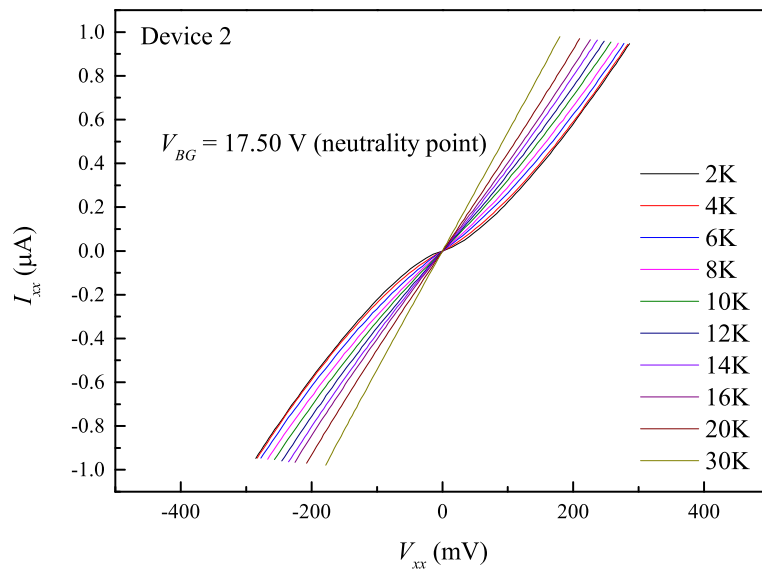


Figure A.2: Temperature dependence for D2 at the neutrality point ($V_{BG} = 17.5$ V).

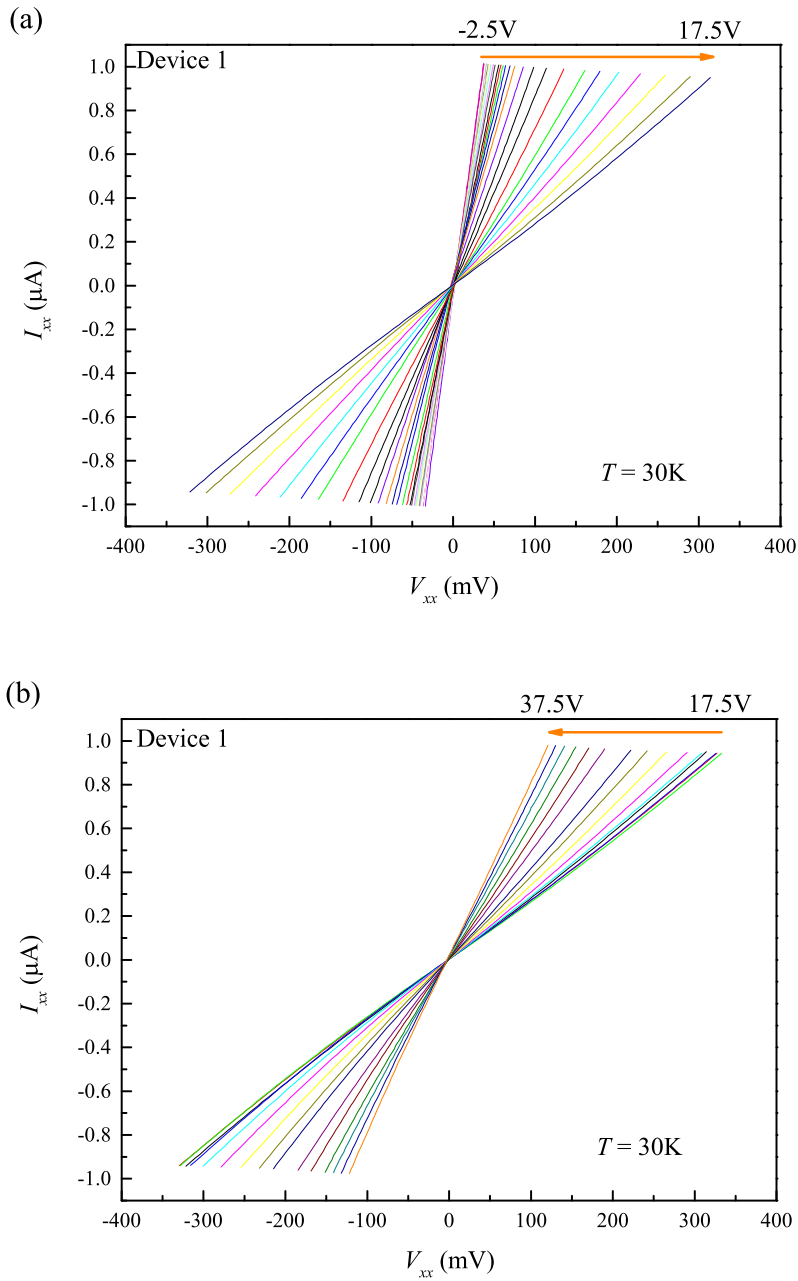


Figure A.3: I - V curves for D1 at 30K. (a) and (b) are in the hole and the electron region respectively. The back gate voltage is set at $-2.5, 0, 2.5, 5, 7.5, 8.75, 10, 11.25, 12.5, 13.75, 15, 16.25, 17.5\text{ V}$ from left to right for figure a; $17.5, 18.75, 20, 21.25, 22.5, 23.75, 25, 27.5, 30, 32.5, 35, 37.5\text{ V}$ from right to left for figure b.

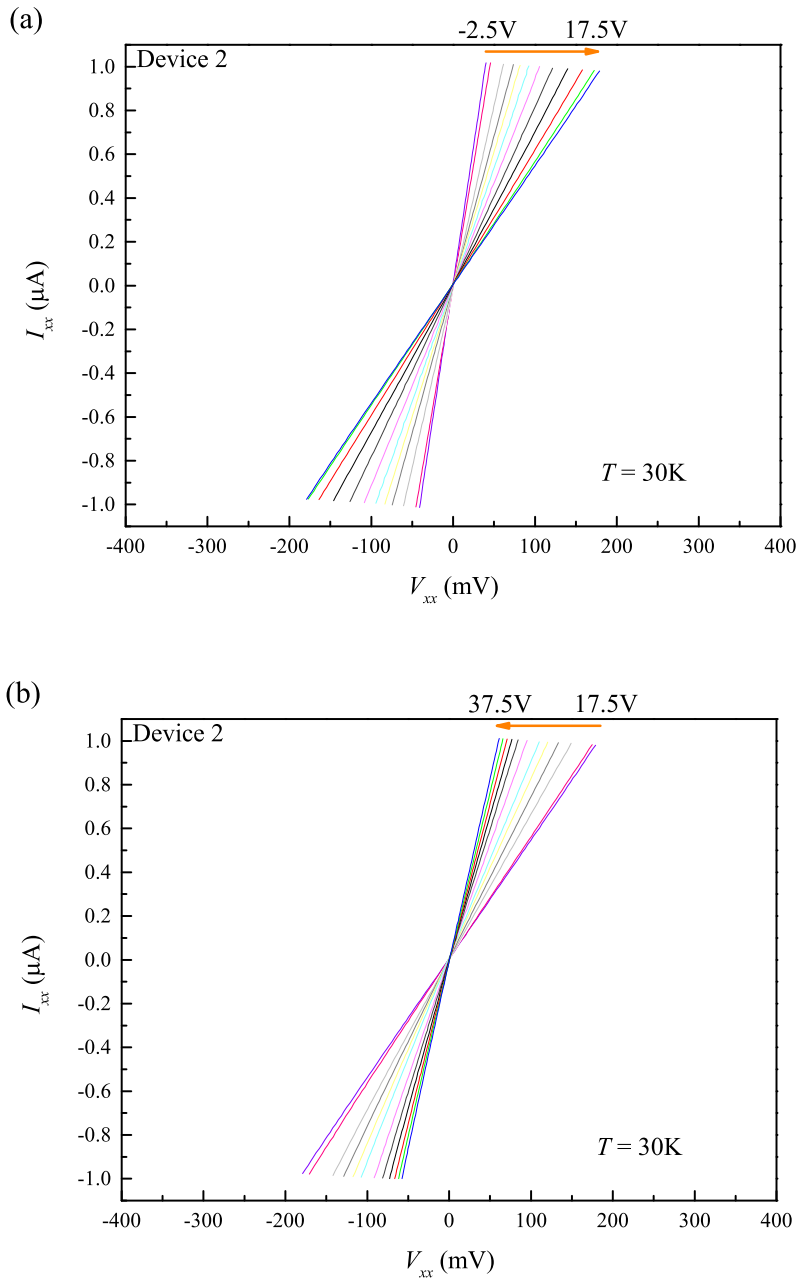


Figure A.4: I - V curves for D2 at 30K. (a) and (b) are in the hole and the electron region respectively. The back gate voltage is set at $-2.5, 0, 2.5, 5, 7.5, 8.75, 10, 11.25, 12.5, 13.75, 15, 16.25, 17.5$ V from left to right for figure a; $17.5, 18.75, 20, 21.25, 22.5, 23.75, 25, 27.5, 30, 32.5, 35, 37.5$ V from right to left for figure b.

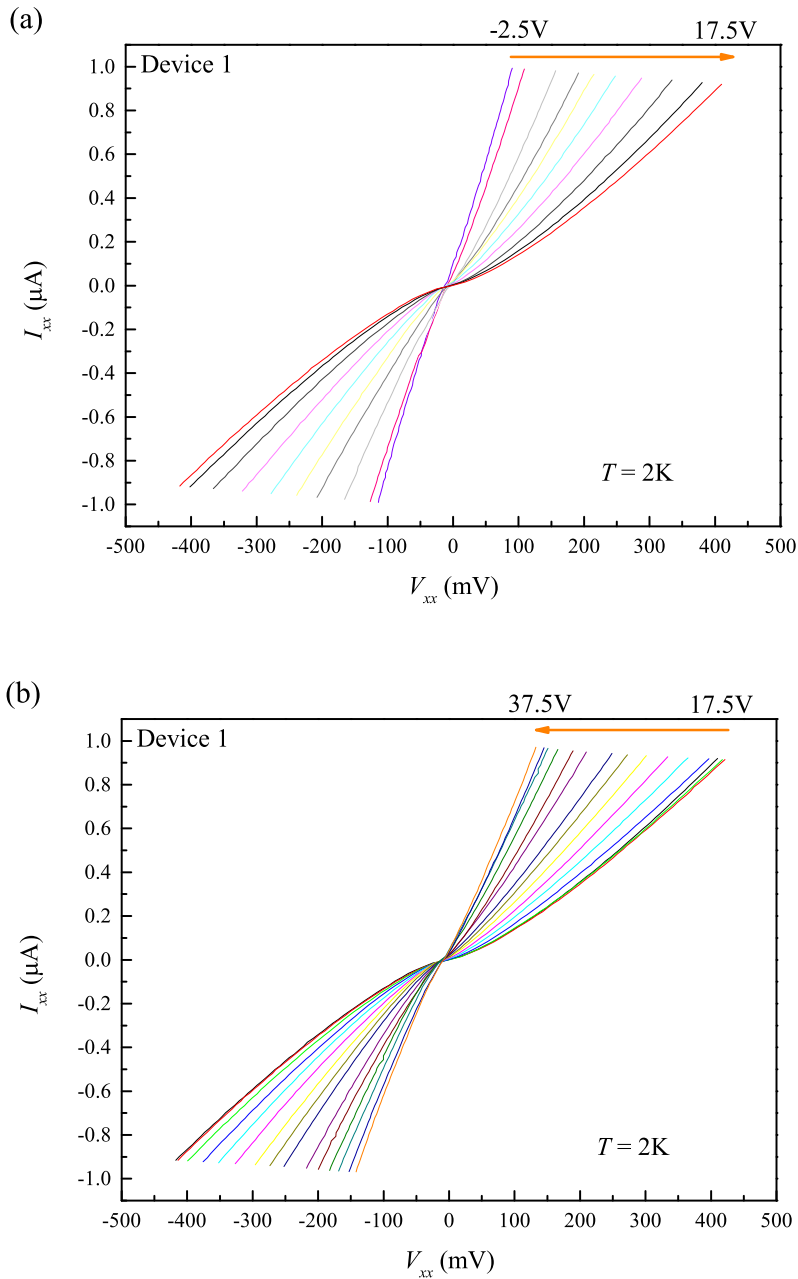


Figure A.5: I - V curves for D1 at 2K. (a) and (b) are in the hole and the electron region respectively. The back gate voltage is set at $-2.5, 0, 2.5, 5, 7.5, 8.75, 10, 11.25, 12.5, 13.75, 15, 16.25, 17.5\text{ V}$ from left to right for figure a; $17.5, 18.75, 20, 21.25, 22.5, 23.75, 25, 27.5, 30, 32.5, 35, 37.5\text{ V}$ from right to left for figure b.

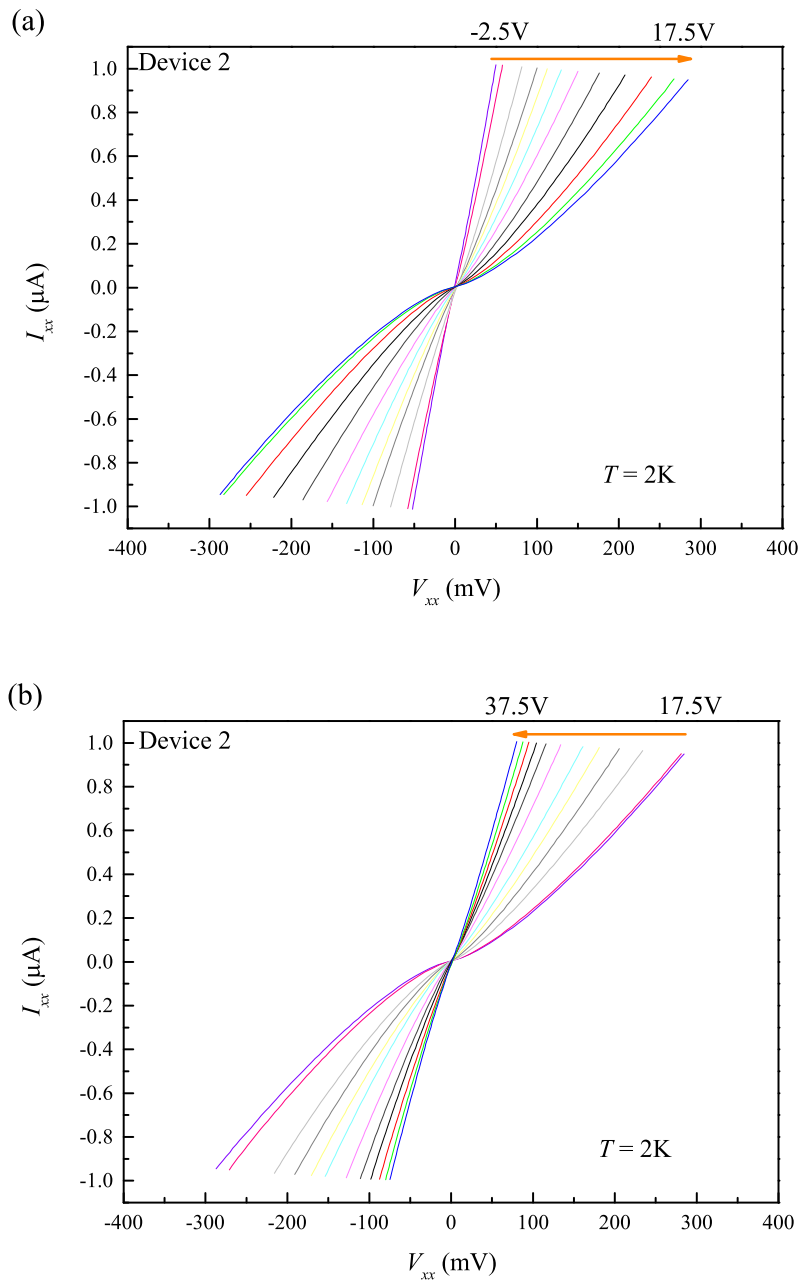


Figure A.6: I - V curves for D2 at 2K. (a) and (b) are in the hole and the electron region respectively. The back gate voltage is set at $-2.5, 0, 2.5, 5, 7.5, 8.75, 10, 11.25, 12.5, 13.75, 15, 16.25, 17.5$ V from left to right for figure a; $17.5, 18.75, 20, 21.25, 22.5, 23.75, 25, 27.5, 30, 32.5, 35, 37.5$ V from right to left for figure b.



Appendix B

Temperature Dependence on the Conductance for D3

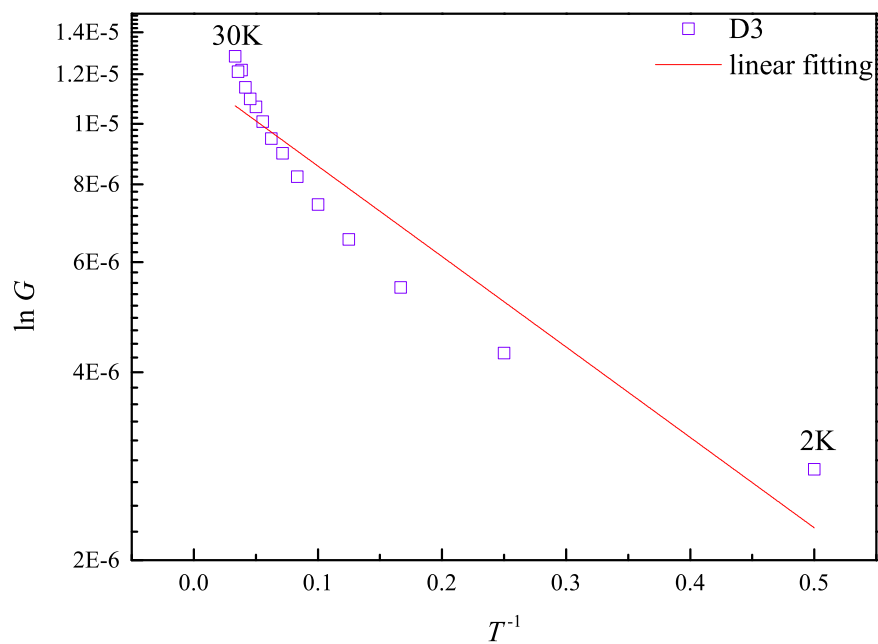


Figure B.1: $\ln G$ versus T^{-1} by thermal activated model, which follows $G(T) = G_0 \exp(-\frac{T_0}{T})$.

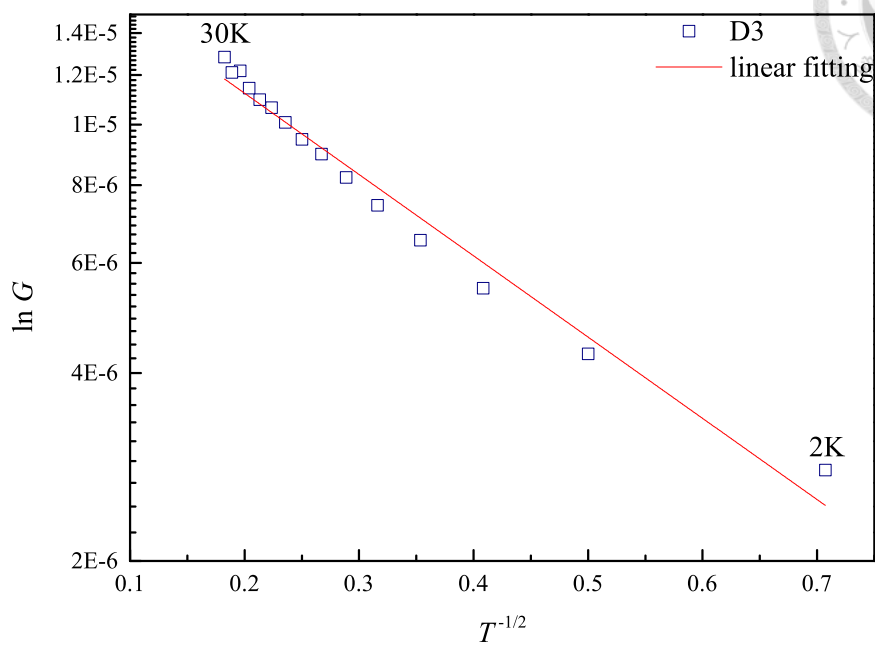
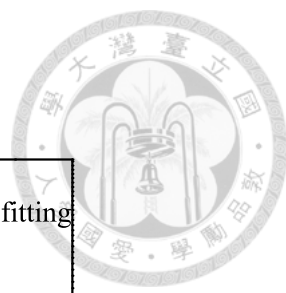


Figure B.2: $\ln G$ versus $T^{-1/2}$ by ES VRH model, which follows $G(T) = G_1 \exp(-\frac{T_0}{T})^{1/2}$ for 2D system.

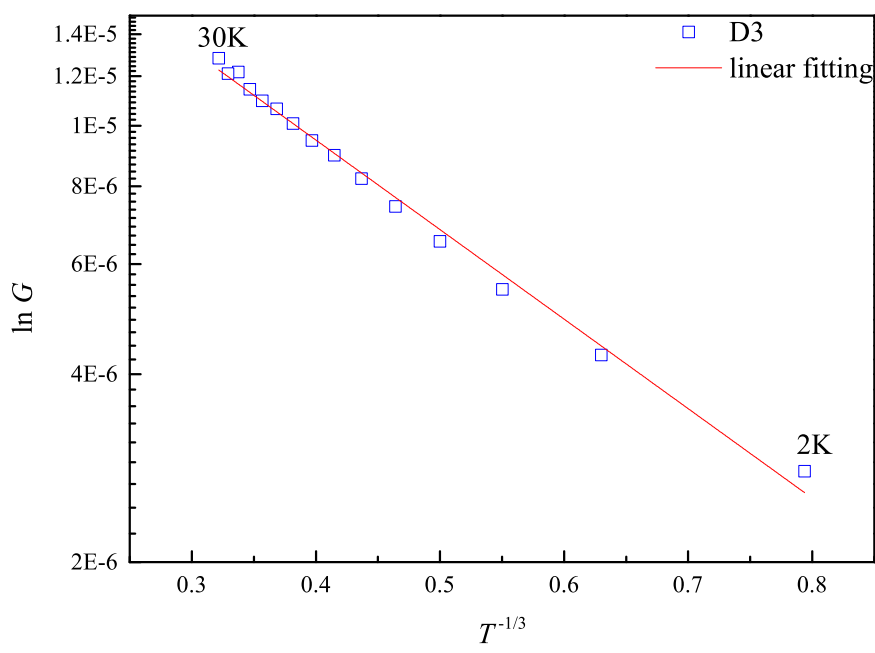


Figure B.3: $\ln G$ versus $T^{-1/3}$ by Mott VRH model, which follows $G(T) = G_2 \exp(-\frac{T_0}{T})^{1/3}$.



Appendix C

Strength of disorder by Raman spectroscopy

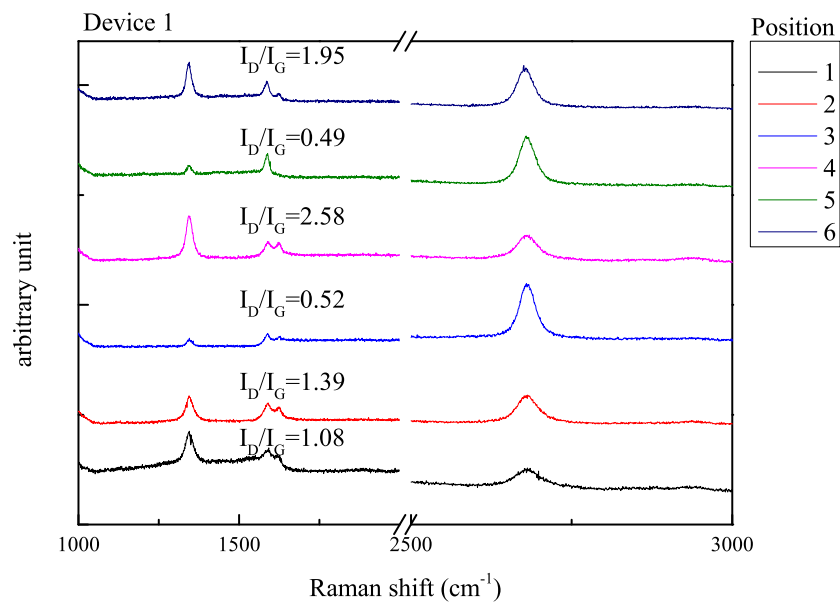


Figure C.1: The intensity of the disorder by Raman spectroscopy for D1. An offset has been added in order to separate each line. The value of I_D/I_G for each line is labels on the graph.

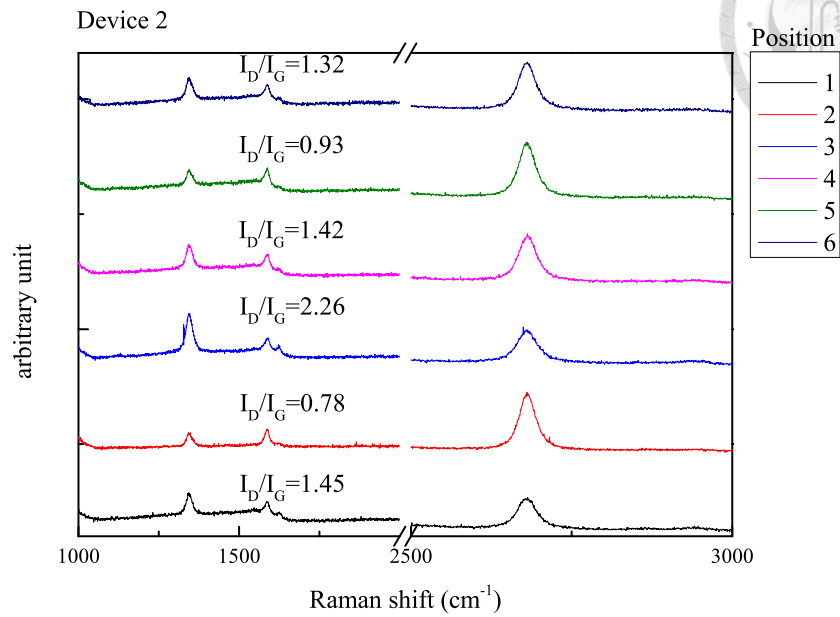


Figure C.2: The intensity of the disorder by Raman spectroscopy for D2. An offset has been added to in order to separate each line. The value of I_D/I_G for each line is labels on the graph.

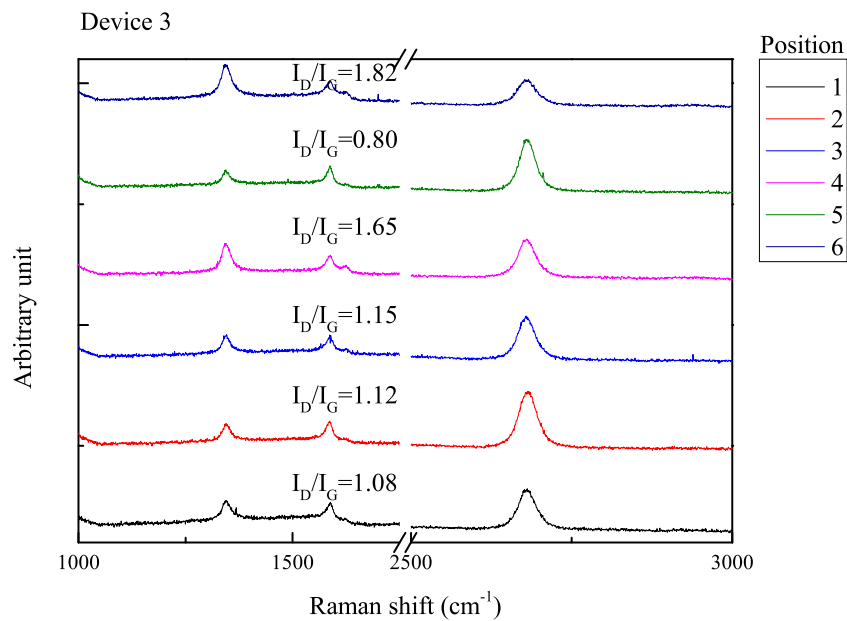


Figure C.3: The intensity of the disorder by Raman spectroscopy for D3. An offset has been added to in order to separate each line. The value of I_D/I_G for each line is labels on the graph.